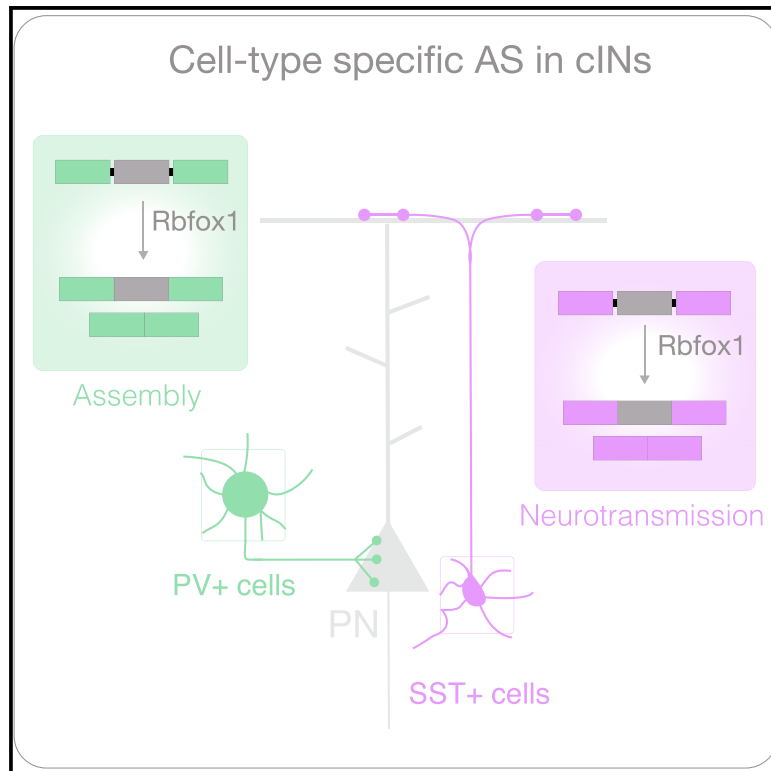


Neuron

Rbfox1 Mediates Cell-type-Specific Splicing in Cortical Interneurons

Graphical Abstract



Authors

Brie Wamsley, Xavier Hubert Jaglin, Emilia Favuzzi, ..., Alireza Khodadadi-Jamayran, Bernardo Rudy, Gord Fishell

Correspondence

gordon_fishell@hms.harvard.edu

In Brief

Wamsley et al. uncover a role of the splicing regulator Rbfox1 in promoting interneuron-specific connectivity in the developing neocortex. By differentially regulating alternative splicing profiles in PV+ and SST+ interneurons, Rbfox1 tailors their efferent connectivity.

Highlights

- Alternative splicing is actively regulated during cortical interneuron development
- Rbfox1 orchestrates cell-type-specific splicing in cortical interneurons
- Rbfox1 is required to establish SST+ and PV+ interneuron connectivity
- Alternative splicing in interneurons directs axonal and synaptic formation



Rbfox1 Mediates Cell-type-Specific Splicing in Cortical Interneurons

Brie Wamsley,^{1,2,5} Xavier Hubert Jaglin,^{1,2,5} Emilia Favuzzi,^{2,3,5} Giulia Quattrocchio,¹ Maximiliano José Nigro,¹ Nusrath Yusuf,^{1,2,3} Alireza Khodadadi-Jamayran,⁴ Bernardo Rudy,¹ and Gord Fishell^{1,2,3,6,*}

¹NYU Neuroscience Institute and the Department of Neuroscience and Physiology, Smilow Research Center, New York University School of Medicine, 522 First Avenue, New York, NY 10016, USA

²Department of Neurobiology, Harvard Medical School, 220 Longwood Avenue, Boston, MA 02115, USA

³Stanley Center at the Broad, 75 Ames Street, Cambridge, MA 02142, USA

⁴Genome Technology Center, Applied Bioinformatics Laboratories, NYU Langone Medical Center, 550 First Avenue, MSB 304, New York, NY 10016, USA

⁵These authors contributed equally

⁶Lead Contact

*Correspondence: gordon_fishell@hms.harvard.edu

<https://doi.org/10.1016/j.neuron.2018.09.026>

SUMMARY

Cortical interneurons display a remarkable diversity in their morphology, physiological properties, and connectivity. Elucidating the molecular determinants underlying this heterogeneity is essential for understanding interneuron development and function. We discovered that alternative splicing differentially regulates the integration of somatostatin- and parvalbumin-expressing interneurons into nascent cortical circuits through the cell-type-specific tailoring of mRNAs. Specifically, we identified a role for the activity-dependent splicing regulator Rbfox1 in the development of cortical interneuron-subtype-specific efferent connectivity. Our work demonstrates that Rbfox1 mediates largely non-overlapping alternative splicing programs within two distinct but related classes of interneurons.

INTRODUCTION

Cellular diversity within the CNS has evolved to support intricate neuronal circuits and a broad range of complex behaviors. Cortical interneurons (cINs) are emblematic of this diversity. Although representing only a small proportion of the cells within the cortex, discrete cIN subclasses are critical for supporting network functions. One remarkable aspect of this diversity is their subtype-specific synaptic connectivity (Blackstad and Flood, 1963). Although the parvalbumin (PV)+ cINs innervate the perisomatic region of pyramidal excitatory neurons, somatostatin (SST)+ cINs preferentially target their distal dendrites. In addition to being useful features for cell classification, these differences in subcellular targeting are critical to their function (Tremblay et al., 2016). However, whether these distinct features are genetically hard-wired, imposed by environmentally driven mechanisms (such as early neuronal activity), or some combination of the two is poorly understood (Wamsley and Fishell, 2017).

Although there is no doubt that transcription regulation is involved in cIN specification and maturation (reviewed in Batista-Brito and Fishell, 2009), it alone seems unlikely to account for the full range of functional diversity within cIN subtypes. Consistent with this idea, neurons utilize a variety of other modes of gene expression regulation to enhance their molecular diversity. These include the differential usage of transcription start sites, alternative RNA splicing, polyadenylation, and editing (Maniatis and Tasic, 2002). Indeed, about 90%–95% of transcripts from human genes undergo alternative splicing (AS) (Johnson et al., 2009; Pan et al., 2008; Wang et al., 2008). Recent genome-wide investigations of AS in mice have highlighted its prevalence during development within various regions of the nervous system (Dillman et al., 2013; Pan et al., 2008; Wang et al., 2008; Yan et al., 2015). Specifically, AS participates in cell fate decisions during cortical neurogenesis (Linares et al., 2015; Zhang et al., 2016), as well as synaptogenesis and synaptic plasticity (reviewed in Raj and Blencowe, 2015; Vuong et al., 2016).

In the present study, we find that AS events play a central role within SST+ and PV+ cINs during their integration into the cortex. We discovered that the number of AS events within these cell types varies as they mature. Moreover, our work indicates that Rbfox1 function is essential in regulating distinct AS events within developing PV+ and SST+ cINs. Together, our findings demonstrate that Rbfox1-mediated AS is essential for the genetic regulation of developing cIN connectivity.

RESULTS

Alternative Splicing Is Actively Regulated during Cortical Interneuron Development

The extent to which AS is differentially regulated in cIN subtypes has not been explored. To address this question, we examined the amount of differentially expressed exons in cINs across developmental time points ranging from embryogenesis (embryonic day 18.5 [E18.5]) to juvenile ages (postnatal day 22 [P22]). We took advantage of the *Tg-Lhx6e::GFP* line, in which GFP is constitutively expressed in medial ganglionic eminence (MGE)-derived cINs (PV+ and SST+ INs) at all ages (Figures 1A and 1B). Using



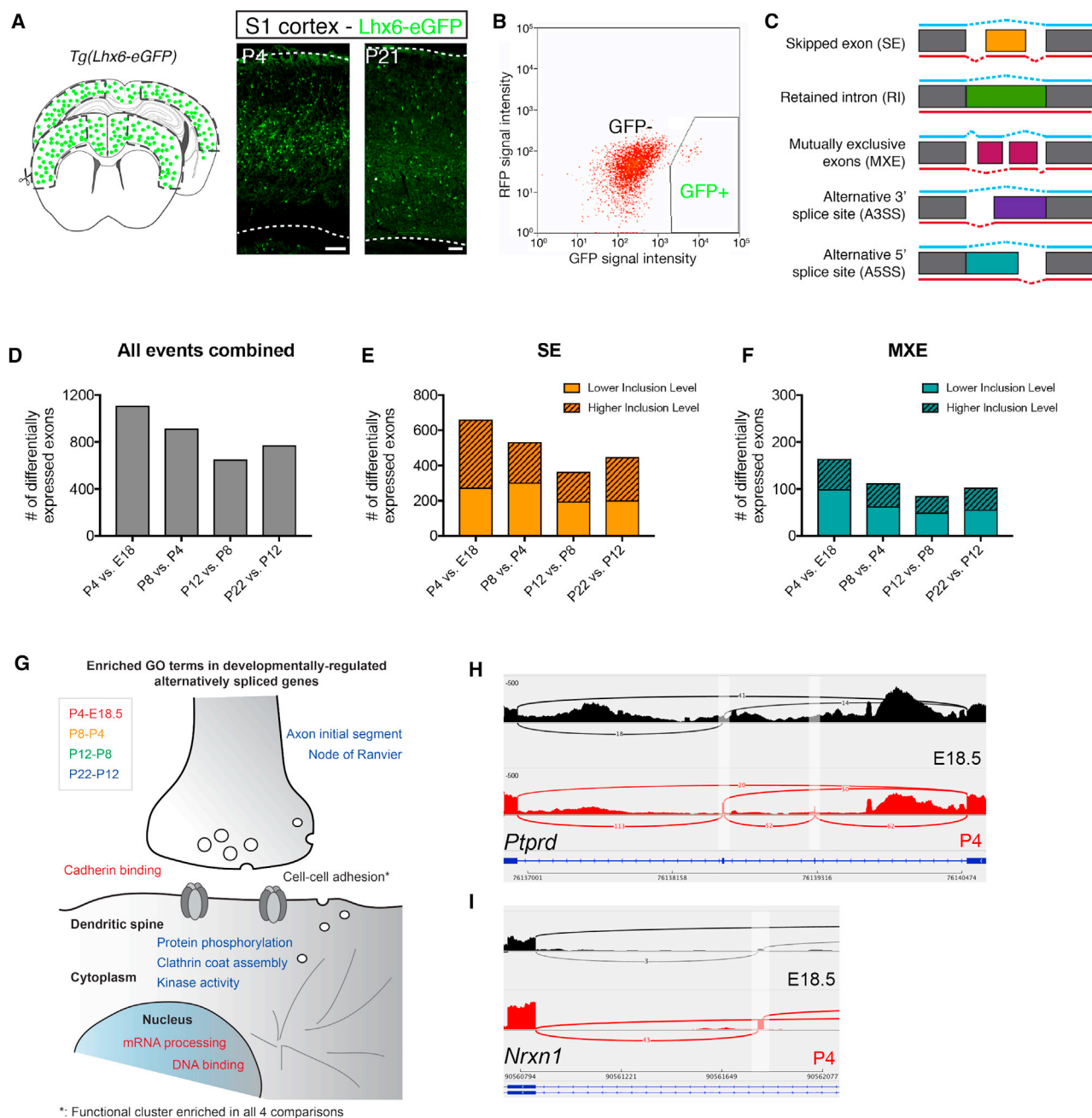


Figure 1. Alternative Splicing Is Dynamically Regulated during MGE cIN Development

(A) Schematic depicting the cortical region isolated from P21 transgenic mouse brains. Corresponding regions were dissected from E18.5, P4, P8, and P12 brains. Examples of the MGE cINs revealed by immunostaining from P4 and P21 *Lhx6*::eGFP primary somatosensory cortices (S1) with anti-GFP (green) antibody are shown.

(B) Fluorescence-activated cell sorting of GFP+ interneurons from *Lhx6*::eGFP mouse cerebral cortex.

(C) Schematic representing the five AS events detected by rMATS.

(D) (Left) Histogram depicting the number of differentially expressed exons in the following comparisons: P4 versus E18.5; P8 versus P4; P12 versus P8; and P22 versus P12 (rMATS analysis; $p < 0.05$ and $|\Delta\psi| \geq 0.1$).

(E and F) Histograms depicting the number of SEs (spliced exons) (E) and MXEs (mutually exclusive exons) (F) that are either more excluded (skipped; plain color) or included (spliced; patterned color).

(G) Schematic depicting the biological functions of the enriched GO terms in the 4 following comparisons: P4 versus E18.5 (dark red) and P22 versus P12 (blue).

(H and I) Sashimi plots of representative examples of the differentially spliced transcripts *Ptprd* (H) and *Nrxn1* (I) from the P4 (red) versus E18.5 (black) comparisons. Scale bars, (A) 100 μ m. Data shown are averages \pm SEM. See also Figure S1 and Table S1.

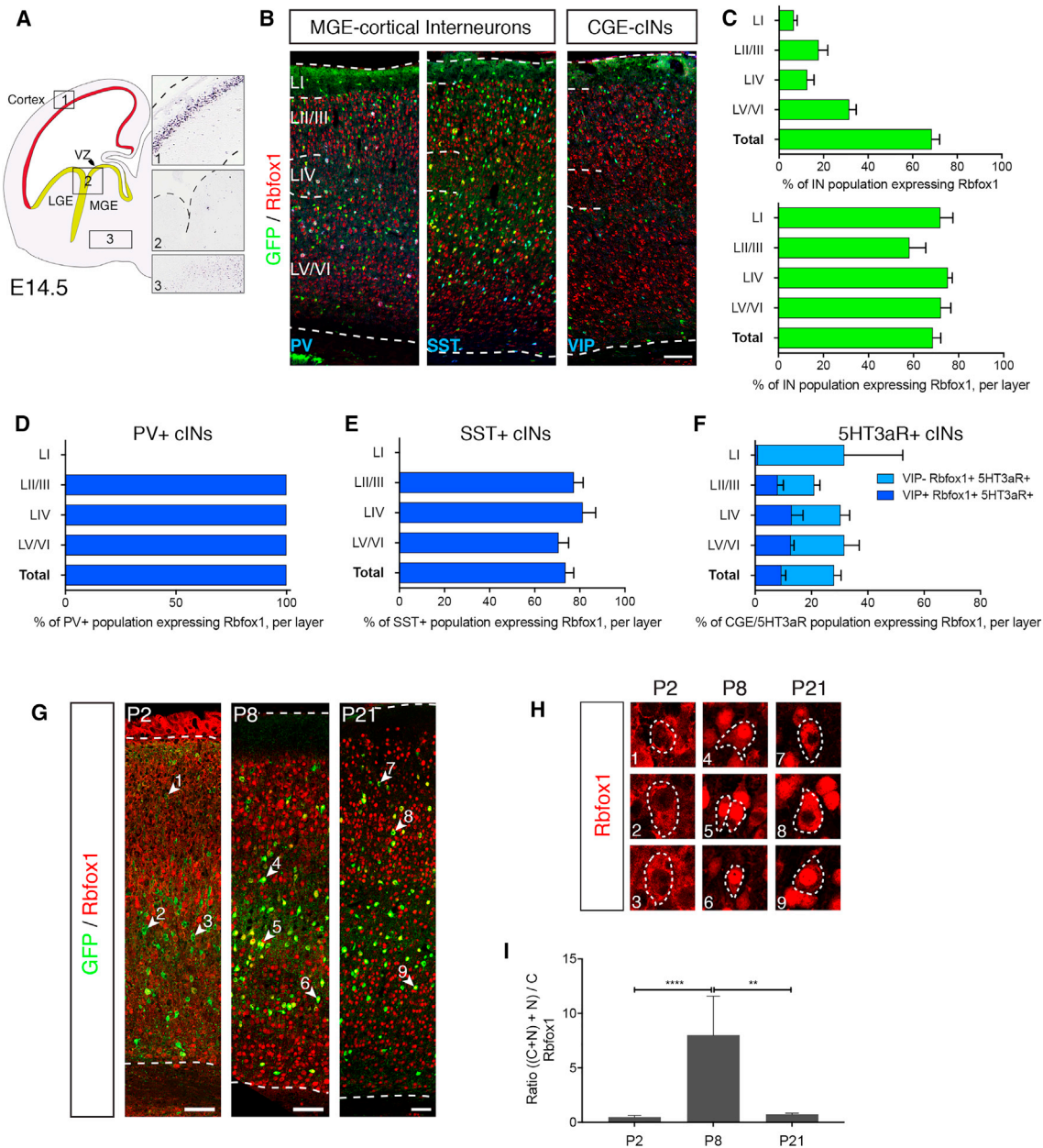


Figure 2. Within Cortical Interneurons, the Splicing Regulator Rbfox1 Is Preferentially Expressed in the PV- and SST-Expressing Subtypes

(A) *In situ* hybridization on an E14.5 mouse embryo (<http://genepaint.org>) revealing that the expression of *Rbfox1* is restricted to postmitotic neurons within the cortical plate and is excluded from the ventricular zones of the dorsal cortex (1) and ganglionic eminences (2). In addition, sparse *Rbfox1*-expressing neurons can be found in the mantle of the ganglionic eminences (3).

(B) Immunostaining of P21 *Dlx6a^{Cre};RCE^{eGFP/+}* (cortical interneurons) and *5HT3aR::eGFP* (CGE cINs) S1 cortices using anti-GFP (green); anti-Rbfox1 (red); and anti-PV (blue, left), anti-SST (blue, middle), and anti-VIP (blue, right).

(C) (Top) Histogram depicting the percentage of the total cIN population (fate mapped using *Dlx6a^{Cre};RCE^{eGFP/+}*) that express Rbfox1 within cortical layers (layer I [LI], layers II-III [LII-III], layer IV [LIV], and layers V-VI [LV-LVI]) and in the whole cortex (total). (Bottom) Histogram depicting the percentage of the cIN population (fate mapped using *Dlx6a^{Cre};RCE^{eGFP/+}*) per layer that express Rbfox1 and in the whole cortex (total).

(D) Histogram depicting the percentage of the PV+-expressing cIN population (fate mapped using *Dlx6a^{Cre};RCE^{eGFP/+}* and stained with anti-PV) that express Rbfox1 in various layers and in the whole cortex (total).

(E) Histogram depicting the percentage of the SST+-expressing cIN population (fate mapped using *Dlx6a^{Cre};RCE^{eGFP/+}* and stained with anti-SST) that express Rbfox1 in various layers and in the whole cortex (total).

(F) Histogram depicting the percentage of the *5HT3aR::eGFP* cIN population (stained with anti-VIP) divided between eGFP/VIP+ (yellow) and eGFP/VIP- (brown) that express Rbfox1 in various layers and in the whole cortex (total).

(legend continued on next page)

fluorescence-activated cell sorting (FACS), we isolated GFP+ MGE-cINs at E18.5, P4, P8, P12, and P22. Sorted cINs were used to prepare cDNA libraries that were subsequently sequenced in order to investigate changes in the prevalence of alternatively spliced exons (spliced exon [SE], mutually exclusive exons [MXE], retained intron [RI], alternative 5' splice site [A5SS], and alternative 3' splice site [A3SS]; Figure 1C). We next examined the pool of genes for which differentially expressed exons or isoforms were observed. Using rMATS (Shen et al., 2014), we found that the number of differentially expressed exons in the *Lhx6*+ population greatly varies throughout development (E18.5 versus P4: 1,109 exons; P4 versus P8: 915 exons; P8 versus P12: 651 exons; P12 versus P22: 772 exons; Figures 1D and S1). Notably, although some of the genes undergoing AS were observed to be spliced at all developmental time points, others show specific developmental profiles (E18.5 versus P4: 49% [414/846 genes]; P4 versus P8: 39% [273/705 genes]; P8 versus P12: 31% [163/530 genes]; P12 versus P22: 37% [222/602 genes]; Figures 1D and S1J). Interestingly, despite changes in gene expression, there were no notable differences in the proportion of the types of splicing events at different developmental time points (i.e., SE, MXE, RI, A5SS, and A3SS; Figures 1E, 1F, and S1A–S1D).

We next examined whether certain gene categories are more likely to be alternatively spliced at specific time points by looking for enrichment of gene ontology (GO) terms across different developmental windows. Analysis between E18.5 and P4 revealed an enrichment of GO terms related to cell-cell adhesion, cadherin binding, mRNA processing, and DNA binding (Figure 1G; Table S1). At later developmental time points (P12 versus P22), the GO enrichment analysis revealed active splicing of genes associated with the following categories: cell-cell adhesion; clathrin coat assembly; protein phosphorylation; kinase activity; and node of Ranvier/axon initial segment (Figures 1G and S1; Table S1). A commonality across all ages is the enrichment for AS genes related to synapse formation and cell-cell adhesion. AS events between E18.5 and P4 appear to be related to initial synaptic establishment and postsynaptic specialization (ex. *Ptprz1*, *Clasp1*, *Nrx1*, and *Ptprd*; Figures 1H and 1I), whereas those enriched between P4 and P8 are involved in axon formation and presynaptic function (ex. *Ntng1*, *Ctnnd1*, *Ank2*, *Cacna1a*, and *Erc2*). Finally, AS events between P12 and P22 are related to protein phosphorylation (ex. *Cask*, *Limk2*, and *Map4k4*) and endocytosis (ex. *Picam* and *Sh3kbp1*; Figure 1G; Table S1).

Rbfox1 Localization in Both PV+ and SST+ Cortical Interneurons Varies during Development

To identify specific factors mediating these AS events, we next surveyed known splice regulators for their expression in cINs.

We identified that the RNA-binding protein fox-1 homolog 1 (Rbfox1) is expressed in post-mitotic precursor cells as early as E14.5 (Figure 2A), a time at which cINs are migrating toward the cortex. Using immunofluorescence and genetic fate mapping, we examined the expression of Rbfox1 within specific cIN subtypes. We observed that the number of Rbfox1-expressing cINs steadily increases during embryonic development up until juvenile stages. By P22, it is expressed in 68.6% ($\pm 9.5\%$) of *Dlx6a*^{cre} fate-mapped cINs within the somatosensory cortex (Figures 2B and 2C). Notably, its expression is enriched in MGE-derived cINs (PV+ cINs: 100%; SST+ cINs: 73.7% $\pm 9.5\%$; Figures 2D and 2E), with relatively fewer caudal ganglion eminence (CGE)-derived cINs expressing Rbfox1 (*5HT3aR::eGFP*: 27.5% $\pm 4.3\%$; Figure 2F).

The *Rbfox1* gene contains several promoters and exons that can result in the generation of multiple isoforms. The nuclear versus cytoplasmic localization of Rbfox1 is controlled by the skipping or inclusion of Rbfox1 mRNA's exon 19. The skipping of exon 19 unveils a cryptic nuclear localization signal (NLS) in downstream exon 20 (Lee et al., 2009). It is this isoform that functions as a splicing regulator (Jin et al., 2003; Nakahata and Kawamoto, 2005; Underwood et al., 2005). Conversely, the cytoplasmic isoform of Rbfox1 (exon 19+) has recently been shown to regulate the stability and enhance the expression level of its target mRNAs (Lee et al., 2016). Given our observation that the number of differentially expressed exons varies during MGE-cIN development, we examined whether Rbfox1 localization also changes. We quantified the relative proportion of *Lhx6*+ MGE-cINs in which Rbfox1 was enriched within the cytoplasm (Rbfox1_C), the nucleus (Rbfox1_N), or in both the nucleus and cytoplasm (Rbfox1_{C+N}) (Figure S1H). We found that, at P2, 67.3% ($\pm 6.5\%$) of *Lhx6::eGFP*+ cINs express Rbfox1_C, 27.3% $\pm 5.3\%$ express Rbfox1_{C+N}, and only 5.5% ($\pm 3.9\%$) express Rbfox1_N (Figures 2G, 2H, and S1I). Interestingly, at P8, we observed a significant increase of the proportion of Rbfox1_{C+N} (86.8% $\pm 7.8\%$) at the expense of Rbfox1_C, whose proportion decreases to 6.50% ($\pm 7.5\%$; Figure S1I). As a consequence of this change in distribution, the ratio of neurons with nuclear Rbfox1 (including Rbfox1_{C+N}) to neurons expressing Rbfox1_C becomes significantly higher (8.00 versus 0.50; Figure 2I). Interestingly, the reduction in Rbfox1_C is transient, as indicated by the enrichment of Rbfox1_C (58.2% $\pm 4.0\%$) at P21, which led to a significant reduction of the N/C ratio (0.73 versus 8.00; Figures 2I and S1I). Altogether, our observations indicate that, at P8, Rbfox1 may be primarily involved in regulating splicing. By contrast, the later enrichment of Rbfox1_C suggests that, in more mature cells (P21), Rbfox1 may additionally regulate mRNA stability (Vuong et al., 2018). Notably, this trend is similar within both SST+ (*Lhx6::eGFP*+ / SST+) and PV+ (*Lhx6::eGFP*+ / SST) cINs over this time period (not shown).

(G) Immunostaining of P2, P8, and P21 S1 cortex from *Lhx6::eGFP* transgenic mice, where MGE-derived cINs are labeled with GFP and stained with anti-Rbfox1 (red). Nine representative GFP+ cINs are labeled with white arrowheads (1–9), and the corresponding higher magnifications pictures are shown in (B).

(H) Higher magnifications illustrate a shift in Rbfox1 localization between P2–P8 and P8–P21 (anti-Rbfox1, red).

(I) The ratios of nuclear Rbfox1 (Rbfox1_N and Rbfox1_{C+N}) over cytoplasmic Rbfox1 (Rbfox1_C) at P2, P8, and P21 in eGFP+ interneurons were determined based on the quantifications shown in Figure S2E (N_{P2} = 16; N_{P8} = 6; N_{P21} = 6). **p < 0.01, ****p < 0.0001.

Scale bars, (B) 100 μ m; (G) 60 μ m. Data shown are averages \pm SEM.

Interneuron-Specific Loss of *Rbfox1* Impairs Cortical Inhibition

We next conditionally inactivated *Rbfox1* by crossing the *Rbfox1*^{F/F} allele (Gehman et al., 2011) with a *Dlx6a*^{Cre} driver line (Yu et al., 2011). This results in the deletion of *Rbfox1* in all cINs during embryogenesis, shortly after they become postmitotic. We took advantage of two different reporter lines, the *RCE*^{LoxP} (referred to as *RCE*^{eGFP}) and *Ai9*^{LoxP} (referred to as *Ai9*^{F/F}), which upon Cre-mediated recombination conditionally express GFP or TdTomato, respectively. We confirmed by immunofluorescence that *Rbfox1* expression is abolished in cINs in the *Dlx6a*^{Cre} conditional knockout (*Dlx6a*^{Cre};*Rbfox1*^{F/F}; *RCE*^{eGFP}; henceforth referred to as *Dlx-cKO*; Figure S2A). We observed that *wild-type* (WT), *Dlx-het*, and *Dlx-cKO* are born at the expected Mendelian ratios (1:2:1; not shown). However, subsequently, we observed an increased lethality of *Dlx-cKO* mice beginning at P18, although both WT and *Dlx-het* show normal survival (Figure S2B). All *Dlx-cKO* mice were deceased by P45. In several instances, we observed *Dlx-cKO*s spontaneously experiencing seizures in their home cage, suggesting that the shortened lifespan observed was caused by lethal seizures. To determine whether *Dlx-cKO*s exhibited increased seizure susceptibility, we monitored the behavior of P12–P14 WT and *Dlx-cKO* mice following intraperitoneal injections of kainic acid (KA) (12 mg/kg) and scored their behavior over a 70-min period according to a modified Racine scale (Gehman et al., 2011; Racine, 1972). We found that KA elicited *status epilepticus* and death in *Dlx-cKO* mice within 30 min, and WT mice experienced mild seizures (2/9 mice displayed forelimb clonus) and eventually recovered (Figure S2C). Notably, heightened seizure susceptibility similar to what we observed in *Dlx-cKO* mice has been reported in adult mice following the pan-neuronal removal of *Rbfox1* using the *Nestin*^{Cre} (Gehman et al., 2011). This suggests that both the pan-neuronal and the cIN-specific loss of *Rbfox1* heightens seizure susceptibility and potentially impairs inhibition. However, the interneuron-specific model is more severely affected, as suggested by the early lethality observed in *Dlx-cKO* mice.

The literature abounds with examples where reductions in cIN numbers result in seizures (Lodato et al., 2011; Marin, 2012). However, we did not find a reduction in cINs. To the contrary, we found a slight increase in PV+ and SST+ cIN density, suggesting a decrease in cell death (Priya et al., 2018; Figures S2D–S2G). The seizure susceptibility in *Dlx-cKO* mice in the absence of a loss of interneurons suggested that inhibitory function was compromised in these animals. To examine this issue in greater detail, we assessed inhibitory currents in the somatosensory cortex using whole-cell patch-clamp recording in acute slices of both juvenile *Rbfox1* *Dlx-cKO* and *Dlx-control* littermates (aged P15–P18). We recorded and analyzed the level of inhibition received by pyramidal neurons in LII–LIII. We observed a significant reduction in both the frequency (3.12 ± 0.53 Hz in *Dlx-cKO* versus 4.86 ± 0.42 Hz in *Dlx-control*) and amplitude (median amplitude: 13.10 pA in *Dlx-cKO* versus 14.72 pA in *Dlx-control*) of miniature inhibitory postsynaptic currents (mIPSCs) in the mutant brains (Figures 3A and 3B). Consistent with a loss of inhibition and seizure activity, we detected a substantial increase in the expression of activity-dependent immediate early gene cFos (Figures 3C and 3D) and the neuropeptide NPY (not shown) in all

cells. In sum, *Dlx-cKO* mice display impairments in inhibitory function in the cortex that likely explain the increased seizure susceptibility.

Rbfox1 Inactivation in SST+ and PV+ Cortical Interneurons Impairs Their Efferent Connectivity

Epileptic phenotypes have previously been reported to be due to altered maturation of the intrinsic properties of MGE-derived cINs (Batista-Brito et al., 2009; Close et al., 2012). In order to test whether the physiological membrane properties of MGE cINs are affected by the cell-autonomous removal of *Rbfox1*, we generated SST+ and PV+ interneuron-specific *Rbfox1* conditional mutants using *SST*^{Cre} (*SST-cKO*s) and *Tac1*^{Cre} (*Tac1-cKO*s) drivers, respectively (Harris et al., 2014; Taniguchi et al., 2011). The *Tac1*^{Cre} driver allows the targeting of a subset of LII–LIII ($46.5\% \pm 11.1\%$) and LV–LVI ($52.3\% \pm 10.3\%$) PV+ cINs earlier than the standard *PV*^{Cre} drivers (Figures S3A and S3B). As 24% of *Tac1*^{Cre}-targeted cells are not cINs (likely pyramidal neurons; not shown), we used an intersectional genetic strategy to confine our analysis to PV+ cINs. We employed the *Dlx5/6*^{FlpE} allele, which drives the expression of the FlpE recombinase in all cINs, and the *Tac1*^{Cre} driver allele in combination with the intersectional TdTomato-reporter *Ai65*. Using this approach, we first examined their firing (first spike characteristics and maximum firing frequency; rheobase) and passive membrane properties (input resistance) using targeted whole-cell patch-clamp recordings in acute slices of juvenile (aged P15–P18) *SST-* or *Tac1-cKO* versus control littermates (*Tac1-cKO*: 8 HET and 13 MUT; *SST-cKO*: 13 HET and 15 MUT). Most parameters were unaffected in *SST*-conditional *Rbfox1* mutants, with the exception of an increased maximum firing frequency in *SST-cKO*s as compared to *SST-controls* (107 ± 7 Hz versus 85 ± 7 Hz in *SST-cKO* versus *SST-control*; Table S2). The examination of *Tac1-cKO* cINs did not reveal any significant alteration of their active or passive electrophysiological properties (Table S2).

As we did not identify major defects within the intrinsic properties of PV+ and SST+ cINs, we explored whether the loss of inhibitory drive in *Dlx-cKO* mutants reflects defects in the synaptic connectivity of these populations (Figure 4A). We used conditional genetic reporters and cell-type-specific synaptic markers to determine whether efferent synapses from PV+, SST+ cINs, or both were affected. To examine this question within PV+ cINs, we took advantage of the PV+ IN-specific expression of the presynaptic protein synaptotagmin-2 (Sytx2) (Sommeijer and Levelt, 2012) for analyzing PV+ axon terminals in *Dlx-cKO* at weaning age (P19–P23). Using immunohistochemistry, confocal imaging, and puncta analysis (Ippolito and Eroglu, 2010), we quantified the number of Sytx2+ puncta that co-localized with the postsynaptic marker gephyrin within perisomatic regions of LII–LIII and LV–LVI pyramidal neurons. We observed that the removal of *Rbfox1* caused a reduction in the number of PV-specific synapses comparing controls to mutants (0.343 ± 0.012 a.u. and 0.216 ± 0.008 a.u., respectively; Figures 4B, 4C, and S3C). Hence, the reduction of PV-specific inhibitory synapses likely accounts at least in part for the reduced mIPSC frequency.

We next tested whether a later removal of *Rbfox1* results in a similar phenotype using *PV*^{Cre} driver mice. Expression of the

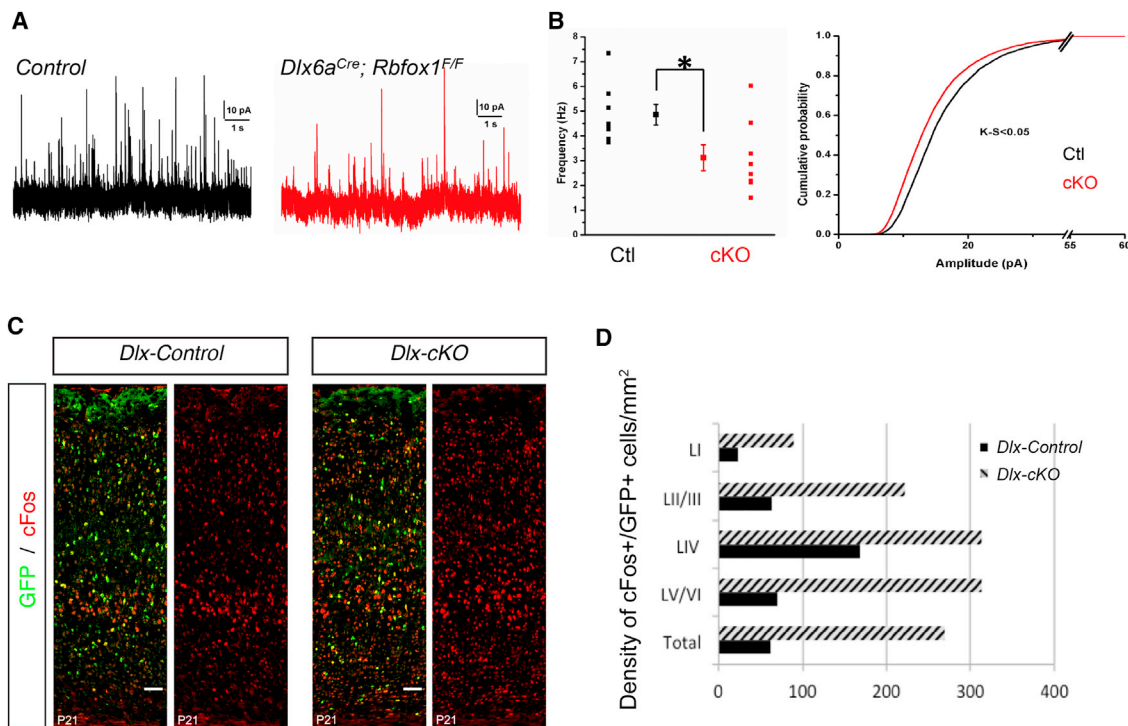


Figure 3. The Interneuron-Specific Inactivation of *Rbfox1* Impairs Inhibitory Function within the Cortex

(A) Representative mIPSCs recorded from LII–LIII pyramidal neurons in control (*Dlx-control*; black) and *Dlx-cKO* (red) cortex at P17 and P18. (B) (Left) Averaged mIPSC frequency between *Dlx-control* and *Dlx-cKO* is reduced ($N_{Dlx-cKO} = 8$ and $N_{Control} = 8$; $p = 0.02$). (Right) Cumulative probability of mIPSC amplitudes from the recorded pyramidal excitatory neurons is also reduced (Kolmogorov–Smirnov test; $*p < 0.05$). (C) Immunostaining of S1 cortex at P21 using anti-GFP (green) and anti-cFos (red) antibodies in the *Dlx-control* and *Dlx-cKO* backgrounds. (D) Associated quantification of cFos+/GFP+ interneurons across cortical layers. Scale bars, (C) 100 μ m. Data shown are averages \pm SEM. See also Figure S2 and Table S2.

Pvalb gene begins around P14 in the somatosensory cortex, resulting in *Rbfox1* inactivation during the third postnatal week, a period following peak synaptogenesis. Notably, we found that the late removal of *Rbfox1* in PV+ cINs did not result in a decrease in the density of Syt2+/gephyrin+ colocalized puncta (Figure S4A) or PV+ cINs (Figure S4B). These results support our hypothesis that *Rbfox1* is critically required during the first two postnatal weeks, coincident with the period of cortical synaptogenesis.

To investigate the consequences of *Rbfox1* genetic inactivation on SST+ cINs efferent synapses, we crossed compound *SST^{Cre};Rbfox1^{F/F}* mice onto a background carrying the conditional presynaptic reporter *Syp-eGFP* (Li et al., 2010). In combination with anti-gephyrin immunostaining, we were able to assess SST+ cortical interneurons' efferent inhibitory synapses. We quantified the number of GFP+/gephyrin+ puncta using confocal imaging in P20–P25 S1 mouse cortex. To our surprise, we observed a significant increase in the amount of SST-cIN synaptic puncta across all layers of the cortex in *SST-cKO*s as compared to control littermates (Figures 4D and 4F–4H; L1: 0.066 ± 0.014 versus 0.116 ± 0.015 and LII–LIII: 0.002 ± 0.001 versus 0.019 ± 0.002 in *SST-control* versus *SST-cKO*, respectively). In particular, we found many more inhibitory synapses in the deeper cortical layers (LV–LVI) of *SST-cKO* than in control

animals (LV–LVI: 0.005 ± 0.001 versus 0.046 ± 0.004 in *SST-control* versus *SST-cKO*). To further ascertain that we are accurately assessing the increase in synapse number in *SST-cKO* animals, we confirmed the juxtaposition of Syp-GFP to both VGAT (vesicular GABA transporter) (Figures 4E and S3D–S3F) or synaptophysin-1 protein using immunocytochemistry (not shown). Altogether, our investigations uncovered distinct but opposing synaptic alterations in PV– versus *SST-cKO* mutants (Figure 4I). Upon the conditional removal of *Rbfox1*, PV+ cINs showed a reduced number of efferent synapses, whereas SST+ cINs form supernumerary inhibitory efferent synapses.

Conditional Loss of *Rbfox1* Reduces Efferent Synaptic Transmission from SST+ Cortical Interneurons

To reconcile the increased density of efferent synapses in *SST-cKO* mutants with the observed reduction in inhibitory drive, we examined whether the extra synapses we observed were functional. In order to assess the synaptic output from SST-cINs onto pyramidal neurons, we employed an optogenetic-based approach. Channelrhodopsin2 (ChR2) was expressed in SST+ interneurons using the Ai32 conditional ChR2-expressing reporter (*Ai32^{F/F}*). We applied single 1-ms blue light stimulations (470 nm) of varying intensities onto LII–LIII of somatosensory cortical slices and analyzed averaged resultant IPSCs within

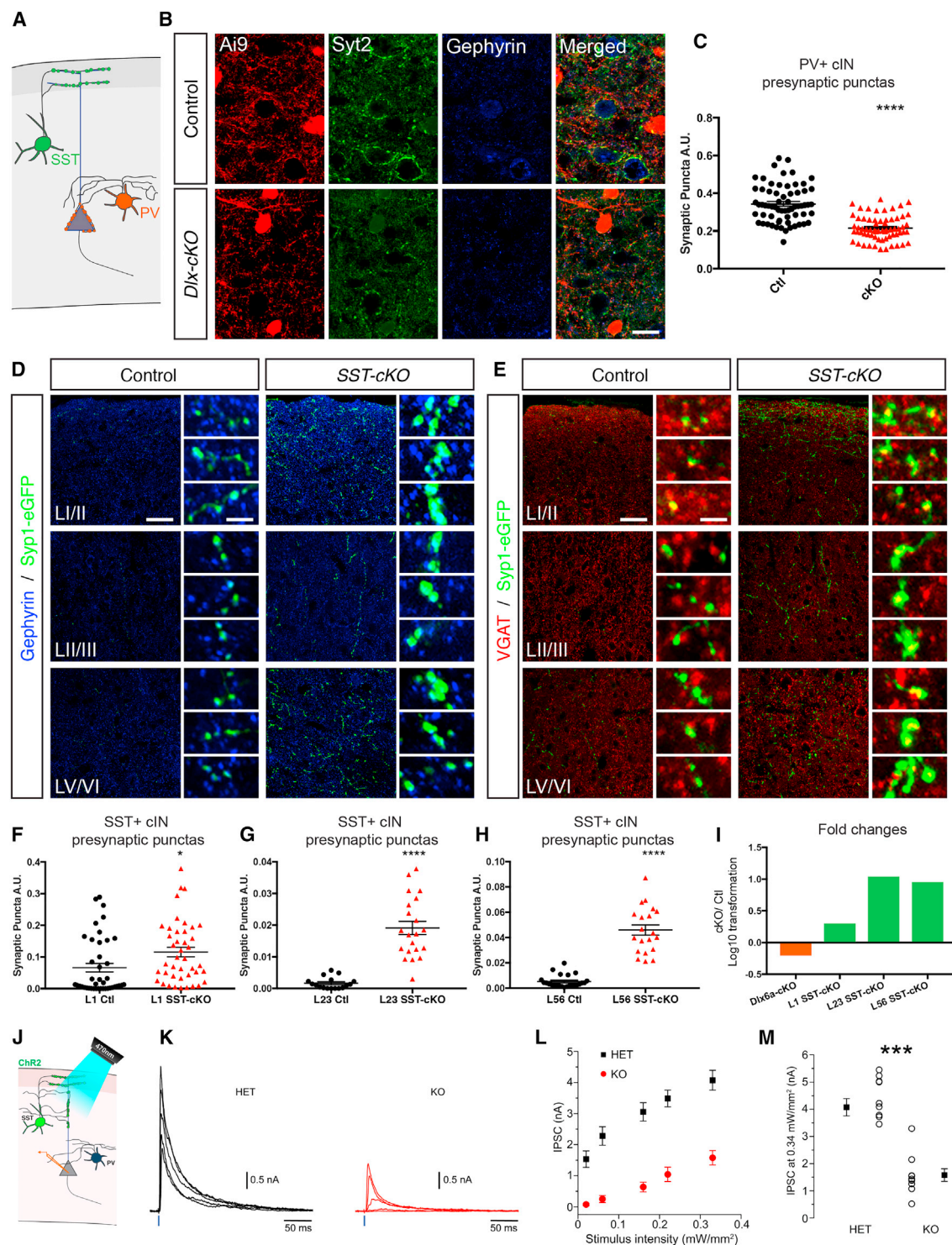


Figure 4. Inactivation of Rbfox1 Has Opposing Effects on Somatostatin+ and Parvalbumin+ cIN Efferent Connectivity

(A) Schematic illustrating the subcellular targeting of SST+ cIN efferent synapses on apical dendrites of pyramidal neurons (green) and of PV+ cIN efferent perisomatic synapses onto pyramidal neurons (orange).

(B) Immunostaining of *Dlx-control* and *Dlx-cKO* cortex with anti-dsRed (red), anti-Syt2 (green), and anti-gephyrin (blue).

(C) Quantification of Ai9/Syt2/gephyrin puncta in both control and *Dlx-cKO* at P17 and P18 reveals a reduction in PV+ cIN efferents ($N_{Dlx-cKO} = 65$; $N_{Dlx-Control} = 65$).

**** $p < 0.0001$.

(legend continued on next page)

pyramidal neurons. We observed a dramatic reduction of inhibitory neurotransmission from SST+ cINs in SST-cKO adult slices (Figures 4J–4M; 4.1 ± 0.3 nA versus 1.6 ± 0.2 nA; $p = 5.35E-6$). To determine whether the increased number of efferent SST+ cIN synapses was developmental or compensatory in nature, we analyzed the quantity of synaptic puncta at an earlier age (P8) and found that the number of inhibitory puncta was unchanged (Figures S4C and S4D). This suggested that the super-numerary SST+ synapses represent a homeostatic compensation resulting from the lack of functional SST cIN axon terminals.

Rbfox1 Mediates Alternative Splicing of Transcripts Encoding Presynaptic Proteins

To investigate alterations in gene expression and AS among transcripts within PV and SST cIN subtypes, we selectively sorted these populations from *Rbfox1* conditional mutant and control animals at P8, a developmental stage that corresponds to the peak of synaptogenesis. This also represents a time point when *Rbfox1* is predominantly localized within the nucleus of these cINs. We first examined whether loss of *Rbfox1* affected gene expression. In SST-cKOs, we identified the upregulation and the downregulation of only 2 and 4 genes, respectively (Table S3; $|\text{Log2FC}| > 1$; p value < 0.01). By contrast, the *Tac1* inactivation of *Rbfox1* caused substantial changes in gene expression. We observed 11 up- and 192 downregulated genes, respectively (Table S3; $|\text{Log2FC}| > 1$; $p < 0.01$).

We next examined how the selective loss of *Rbfox1* in SST-cKO and *Tac1*-cKO affected AS. Using rMATS analysis, we identified 305 exons within SST+ cINs that were alternatively spliced due to the inactivation of *Rbfox1* (Figures 5A and 5B; Table S5). GO analysis carried out on the 278 genes displaying one or more *Rbfox1*-dependent splicing changes revealed a significant enrichment of genes with synaptic function (Figures 5C and 5E; Table S4). Similar analysis of the *Tac1*-specific inactivation of *Rbfox1* affected the splicing of 742 alternatively spliced transcripts (Figures 5A and 5B; Table S5). In this case, GO term enrichment analysis revealed 580 differentially spliced genes that were preferentially associated with cell-cell adhesion (Figures 5D and 5E; Table S4).

We observed that a large proportion of alternatively spliced transcripts within SST+ and PV+ cINS—58% (162/278) and 50% (288/580), respectively—had not been previously identified as direct nuclear *Rbfox1* targets in the adult forebrain (Figures 5F and 5G; Damianov et al., 2016). It is possible that some of the

identified transcripts without reported *Rbfox1* direct binding might be differentially spliced only as an indirect consequence of *Rbfox1* inactivation. Notably, we found that transcripts coding for other *trans*-acting RNA splicing regulators, such as *Elavl4* (Figure 5C), were differentially spliced as a result of *Rbfox1* inactivation. Thus, it is likely that the loss of *Rbfox1* also indirectly alters AS patterns indirectly by impacting *Elavl4* function. Of note, previous work examining the pan-neuronal (i.e., *Nestin*^{Cre}) removal of *Rbfox1* (Gehman et al., 2011) identified 31 transcripts whose AS was altered, and of these, only very few were identified within our analysis (1/31 in SST-cINs and 7/31 in PV-cINs; Figure 5G). However, given the small proportion of cINs within the cortex, it remains a possibility that PV+ and SST+-specific *Rbfox1*-dependent events were simply undetected in previous investigations of whole cortical tissue.

In humans, *RBFOX1* is recognized to be associated with autism spectrum disorders (Martin et al., 2007; Sebat et al., 2007), epilepsy, and intellectual disability (Bhalla et al., 2004). Given the enrichment of autism spectrum disorder (ASD)-associated genes identified as *RBFOX1*/*Rbfox1* targets (Voineagu et al., 2011; Weyn-Vanhenryck et al., 2014), we investigated whether AS in PV+ and SST+ cKO mutants preferentially affected ASD candidates. We hence examined the level of overlap between our putative *Rbfox1* targets and the 686 murine orthologs of ASD candidate genes (SFARI gene 2.0; Abrahams et al., 2013). We found that 10% (28/278, SST-cINs and 58/580, PV-cINs) of the genes we identified in either cell type are known ASD candidate genes (Figure 5G). This level of enrichment is comparable to the enrichment previously reported using pan-neuronal genetic manipulations (Weyn-Vanhenryck et al., 2014).

Rbfox1 Orchestrates Cell-type-Specific Splicing of Exons in Cortical Interneurons

The conditional removal of *Rbfox1* within either SST+ or PV+ cINs resulted in a total of 1,047 AS events (Figure 6A), 954 events of which were unique to one of the two cell types (Figure 6A). Among these, only a negligible number of events involved genes that were differentially expressed between SST+ and PV+ cINs (0/954 and 90/954 in SST+ and PV+ cINs, respectively). Importantly, this shows that the cell-specific changes in splicing observed upon *Rbfox1* loss of function are not merely a result of differences in gene expression. Of the 93 events that occurred within both SST+ or PV+ cINs, 36 represent exons that were

(D) Immunostaining of SST-control and SST-cKO cortex using anti-GFP (green) and anti-gephyrin (blue) in LI-LII, LII-LIII, and LV-LVI. This staining reveals the presence of Syp-eGFP synaptic reporter fusion protein colocalized or in close apposition with the postsynaptic reporter gephrin.

(E) Immunostaining of SST-control and SST-cKO cortex with anti-GFP and anti-VGAT using anti-GFP (green) and anti-VGAT (red) in LI-LII, LII-LIII, and LIV-LV. This staining reveals the presence of Syp-eGFP synaptic reporter fusion protein colocalized or in close apposition with the presynaptic reporter VGAT.

(F–H) Quantification of GFP/gephyrin puncta in both controls and SST-cKOs at P21 (F) in LI-LII ($N_{\text{Control}} = N_{\text{SSTcKO}} = 42$), (G) in LII-LIII ($N_{\text{Control}} = N_{\text{SSTcKO}} = 21$), and (H) in LV-LVI ($N_{\text{Control}} = N_{\text{SSTcKO}} = 24$). * $p < 0.05$, **** $p < 0.0001$.

(I) Log10 transformations of the synaptic puncta fold-changes observed between cKO and controls and shown in (C) and (F)–(H).

(J) Illustration of the SST+ cIN targeted optogenetics experiment: ChR2 is expressed in SST+ cINs using the Ai32 reporter line. SST+ cIN neurotransmission was activated with 470 nm light stimulation, and the inhibitory response was recorded by whole-cell patch-clamp recordings from LII or LIII pyramidal neurons within the somatosensory cortex.

(K) Representative evoked currents from a control (black trace) and cKO (red trace) mice. IPSCs were evoked by a series of 1-ms steps of increasing light intensity.

(L) Input-output curve representing the amplitude of the IPSC (nA) as a function of the light stimulus intensity (mW/mm^2).

(M) Summary plot of the response to the maximal light intensity. *** $p < 0.001$.

Scale bars, (B) 25 μm ; (D and E) 60 μm ; insets 5 μm . Data shown are averages \pm SEM. See also Figures S3 and S4.

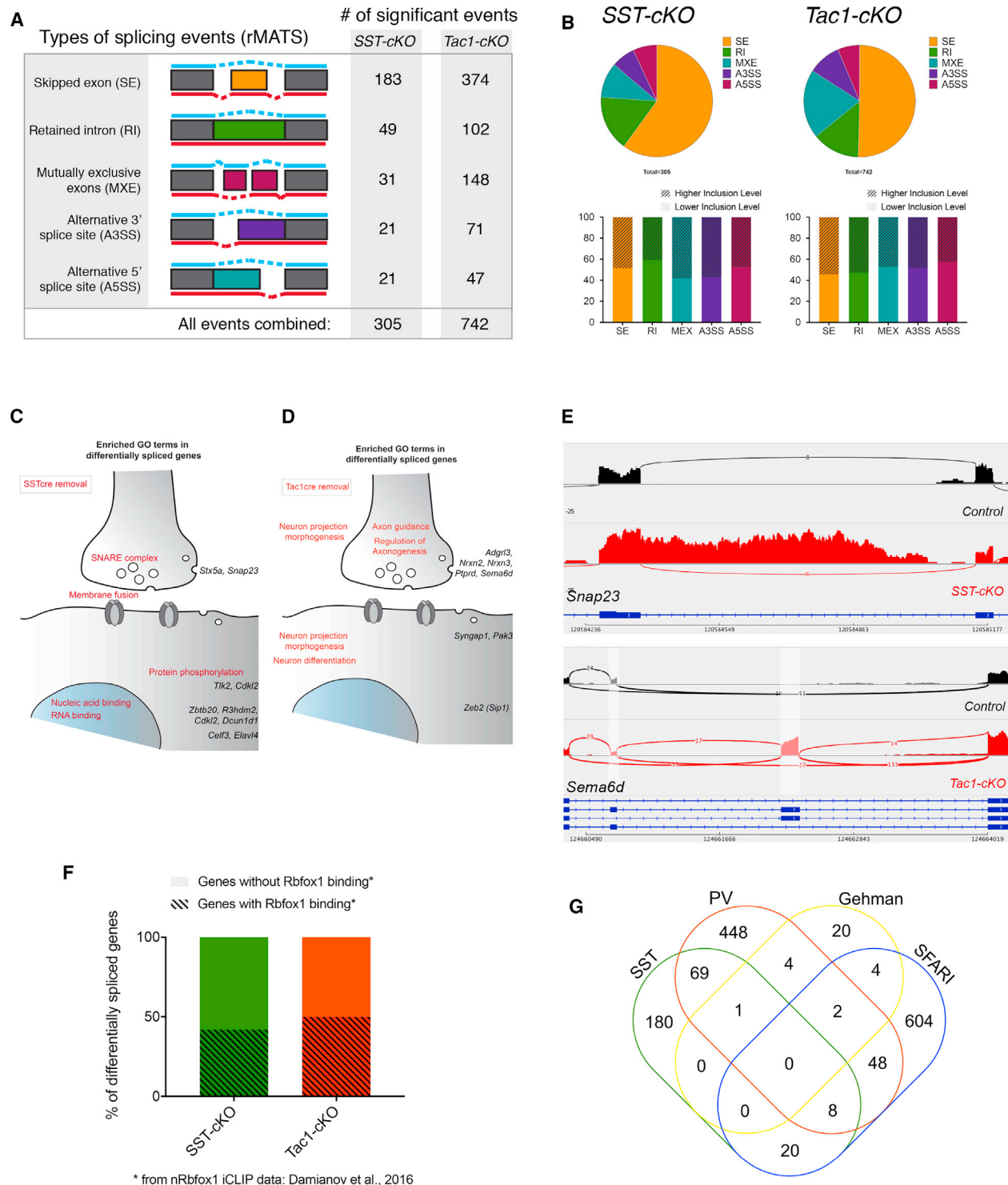


Figure 5. Alternative Splicing Programs in Developing SST+ and PV+ Cortical Interneurons Are Altered upon Loss of *Rbfox1*

(A) Schematic representation of the five types of alternative spliced exon events detected by rMATS and the number of statistically significant events ($p < 0.05$; $|\Delta\psi| > 0.1$) detected within the *SST-cKO* and the *Tac1-cKO* as compared to their respective controls at P8.

(B) (Top) Pie charts showing the breakdown of AS events in the *SST-cKO* (left) and *Tac1-cKO* (right) relative to their respective controls at P8 ($p < 0.05$; $|\Delta\psi| > 0.1$). (Bottom) Proportion of AS events of excluded (plain color) or included target exons (patterned color) in either comparison is shown.

(C and D) Schematics depicting the different biological functions of the enriched GO terms from the set of differentially spliced genes in P8 *SST-cKO* (C) and P8 *Tac1-cKO* cINs (D).

(legend continued on next page)

similarly spliced (or skipped), and 57 reflected cell-type-specific AS outcomes (Figure 6A).

We next sought to confirm that these AS events were altered in a cell-specific manner upon the conditional removal of *Rbfox1*. First, we performed targeted validation experiments in sorted PV+ and SST+ cINs, using fluorescent RT-PCR amplification with primers flanking the alternatively spliced segments (Figures 6C–6H). We successfully validated 18 splicing targets obtaining an ~60%–70% validation rate (Table S6). Additionally, using position weight matrix analysis, we found a significant enrichment of the *Rbfox1* binding motif within close proximity to differentially regulated exons as compared to background unregulated exons (false discovery rate [FDR] > 50%), suggesting that the predicted AS changes result by direct regulation by *Rbfox1* (Figures S6A and S6B). Next, we confirmed that these targets are directly bound and regulated by *Rbfox1* in nuclei preparations (Figures 6B and S6C–S6E). The targets we validated included *Lrrcc1* (leucine-rich repeat and coiled-coil centrosomal protein 1), which encodes a docked synaptic vesicle component enriched at GABAergic synapses (Boyken et al., 2013). Although *Lrrcc1* is expressed in both PV+ and SST+ interneurons, we observed a lower inclusion of the spliced 3' UTR exon in *Tac1*-cKO, but not *SST*-cKO, mice (Figures 6C and 6D). Conversely, we found that the inclusion ratio of exon 4 in *Jakmip3* (Janus kinase and microtubule interacting protein 3) was reduced in *SST*-cKO, but not *Tac1*-cKO, mice (Figures 6E and 6F). Perhaps most strikingly, the AS of exon 18 in *Mttr14* (myotubularin-related protein 14) was differentially altered in the two cell types. Specifically, the absence of *Rbfox1* led to a decreased inclusion in *Tac1*-cKO mice but an increased inclusion in *SST*-cKO mice (Figures 6G and 6H). Altogether, these results confirmed that the changes in AS upon conditional loss of *Rbfox1* are markedly divergent between the two cell populations.

DISCUSSION

Our work highlights the surprising specificity of AS within particular cIN populations and during specific developmental events. In PV+ and SST+ cINs, we observe striking changes in AS during the first three postnatal weeks and demonstrate that this process is both dynamic and exquisitely regulated. We discovered that this process is partially dependent upon *Rbfox1*, which has key cell-type-specific roles during the maturation and integration of discrete cIN classes. Until recently, AS had only been investigated within whole mouse brains or within heterogeneous cellular populations and investigated its role only at set stages (Dillman et al., 2013; Zhang et al., 2014). Recent work has, however, been able to implicate AS in neurogenesis and cell fate determination (Linares et al., 2015; Zhang et al., 2016), synaptic maintenance, and plasticity (Iijima et al., 2011; Nguyen et al.,

2016; and reviewed in Raj and Blencowe, 2015; Vuong et al., 2016). Our work expands upon these efforts by examining the cell-type-specific consequences of AS during specific stages of cIN development. The robust changes in AS between E18.5 and P4 occur concomitantly with the settling of cINs within the cortical layers. This is a period during which they experience an increasingly dynamic range of neuronal activities and are robustly forming or losing synaptic contacts (Allène et al., 2008; Minlebaev et al., 2011; Yang et al., 2009, 2013). The concurrence of AS and activity during these stages of development coupled with the finding that activity alters *Rbfox1* localization (Lee et al., 2009) warrants further investigation.

Our work has also clarified the requirement for *Rbfox1* for brain development. Although the whole brain inactivation of *Rbfox1* causes seizures and results in lethality (Gehman et al., 2011), the neural and molecular bases of these phenotypes was previously unclear. Our work demonstrates that restricting the genetic inactivation of *Rbfox1* to cINs replicates these findings and identifies that an overall reduction of inhibition in the cortex is the likely cause of these phenotypes.

With regard to specific regulatory networks, previous work has shown that *Rbfox1* regulates the splicing of ion channels, neurotransmitter receptors, and cell adhesion molecules (Fogel et al., 2012; Gehman et al., 2011; Lovci et al., 2013; Voineagu et al., 2011; Weyn-Vanhentenryck et al., 2014; Zhang et al., 2008). However, the extent to which targets of AS vary across cell types and across development has remained unclear. The first hint that transcripts were specifically alternatively spliced in individual neurons was suggested over thirty years ago in *Aplysia* (Buck et al., 1987). Since then, few studies have provided examples of particular transcripts being spliced within discrete neuronal populations (Benjamin and Burke, 1994; Fuccillo et al., 2015; Sommer et al., 1990). However, studying how the diversity and regulation of AS patterns is controlled within different cell types has remained technically challenging and to date has mostly been examined in invertebrates (Norris et al., 2014). The striking differences in the *Rbfox1* targets found in PV+ versus SST+ cINs provides insight into how a single splicing regulator can differentially modulate gene expression within two related but distinct cell types. Hence, our findings constitute, to our knowledge, the first evidence of distinct cell-type-specific AS within closely related mammalian neuronal types. It will be interesting to investigate the molecular mechanisms underlying these interneuron subtype-specific AS events. Of note, a role for *Rbfox1* in regulating mRNA stability was recently shown to be important for inhibitory synaptic transmission (Vuong et al., 2018). Although we found that the re-expression of a cytoplasmic-restricted form of *Rbfox1* did not rescue the synaptic phenotypes in cKOs (data now shown), it is still possible that loss of cytoplasmic *Rbfox1* function may contribute to some of the defects observed here.

(E) Sashimi plots of representative examples of differentially spliced transcripts in P8 *SST*-cKO (*Snap23*) and P8 *Tac1*-cKO (*Sema6d*).

(F) Relative fractions of the differentially spliced genes found in either cell type from *SST*-cKOs or *Tac1*-cKOs with or without evidence of nuclear *Rbfox1* direct binding as identified by iCLIP experiment from a nuclear fraction of forebrain neurons (Damianov et al., 2016).

(G) Venn diagram showing the intersection between the sets of differentially spliced transcripts identified in either cell type from *SST*- and *Tac1*-cKOs and the dataset of SFARI ASD-candidate genes and the previously identified set of 30 genes differentially spliced in the adult brain of *Nestin-Cre Rbfox1* conditional KOs (Gehman et al., 2011).

Data shown are averages \pm SEM. See also Figure S5 and Tables S3, S4, and S5.

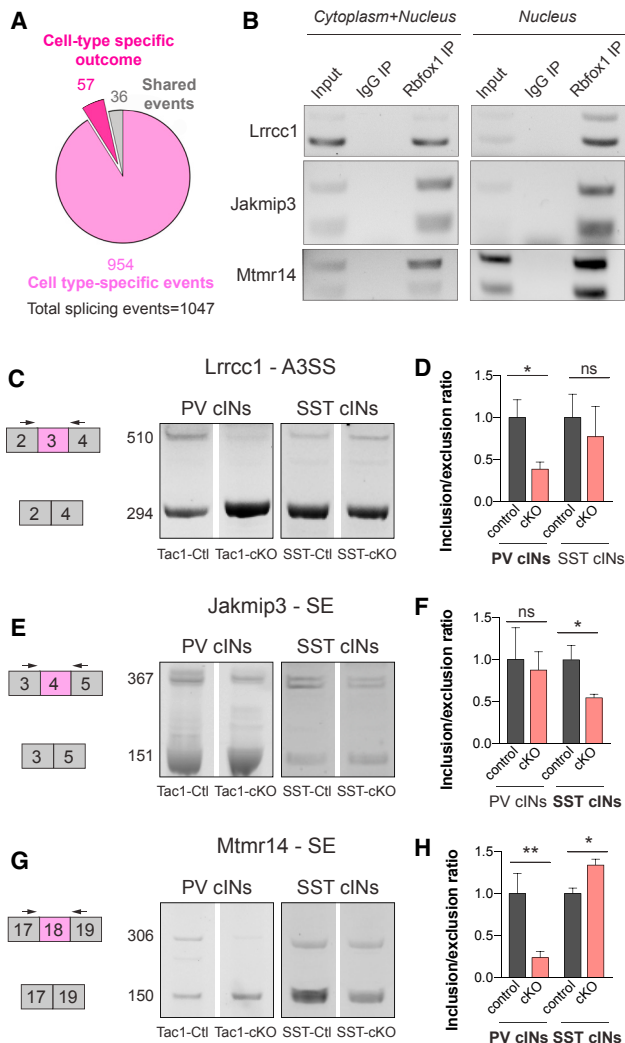


Figure 6. The Splicing Regulator Rbfox1 Governs Cell-type-Specific Alternative Programs in SST+ and PV+ Cortical Interneurons

(A) Pie chart showing the relative proportion of cell-type-specific events (uniquely identified in either SST- or *Tac1*-cKOs or in both SST- and *Tac1*-cKOs but with opposite outcomes) and non-cell-type-specific events. (B) Immunoprecipitation of Rbfox1-RNA complexes in cellular (left) and nuclear (right) extracts. Rbfox1 binds *Lrrcc1*, *Jakmip3*, and *Mtmr14*, three examples of mRNAs from the cell-type-specific outcome category in (A). (C–H) Validation by fluorescent RT-PCR of the indicated Rbfox1 targets. Representative images (C, E, and G) and quantification (D, F, and H) show the inclusion/exclusion ratio (normalized to controls) of Rbfox1-dependent exons in PV+ and SST+ controls versus SST- or *Tac1*-cKOs. Data shown are averages \pm SEM from ≥ 3 biological replicates. * $p < 0.05$, ** $p < 0.01$. See also Figure S6 and Table S6.

Recent work has focused on elucidating the molecular basis for neuronal diversity. In particular, advances in high-throughput genomics and single-cell RNA sequencing (RNA-seq) have for the first time provided a fine grain view of the expression of genes in individual neuronal subtypes and across development (Mayer et al., 2018; Mi et al., 2018; Nowakowski et al., 2017; Tasic et al., 2016, 2017; Zeisel et al., 2015). PV+ and SST+ cINs share a com-

mon developmental history; have a mutual requirement for key genetic factors, including the transcription factors Nkx2-1, Lhx6, Sox6, and Satb1; and arise from a common lineage (Bandler et al., 2017). Our work adds to this by providing a compelling demonstration that, beyond transcriptional differences, some of the unique specializations found within specific cINs rely on differential AS networks, which in part are dependent on Rbfox1.

Mutations of *RBFOX1* are known to be associated with ASD, intellectual disability (ID), and epilepsy (Bhalla et al., 2004; Martin et al., 2007; Sebat et al., 2007). Our understanding of the molecular basis of these disorders has to date relied on global investigations in human brain tissue (Parikshak et al., 2016; Voineagu et al., 2011), constitutive mouse models (Gehman et al., 2011), and knockdown experiments on cultured neurons and cells (Fogel et al., 2012; Lee et al., 2016; Weyn-Vanhentenryck et al., 2014). Our findings, by focusing on the consequences of *Rbfox1* removal in defined cIN classes, illustrate the value of examining the role of disease genes across development and in particular cell types. As such, it will be interesting to further establish the signature of Rbfox1-dependent AS programs within the different neuronal classes that express this gene to gain a clearer image of the causal mechanisms in neurodevelopmental disorders.

STAR★METHODS

Detailed methods are provided in the online version of this paper and include the following:

- KEY RESOURCES TABLE
- CONTACT FOR REAGENT AND RESOURCE SHARING
- EXPERIMENTAL MODEL AND SUBJECT DETAILS
 - Mouse Maintenance and Mouse Strains
- METHOD DETAILS
 - Immunocytochemistry and Imaging
 - Confocal Imaging and Synaptic Puncta Analysis
 - Seizure Susceptibility
 - Electrophysiological Recordings
 - Optogenetic Stimulation
 - Isolation of Cortical Interneurons from the Developing Mouse Cerebral Cortex
 - Nucleic Acid Extraction, RNA Amplification, cDNA Library Preparation, and RNA Sequencing
 - Differential Gene Expression, Alternative Splicing Analyses, and Motif Enrichment
 - Validation of Cell-Specific Rbfox1-Dependent Exons by RT-PCR
 - Immunoprecipitation of RNA-Binding Protein-RNA Complexes (RIP)
 - GO Analysis
 - iCLIP Analysis
- QUANTIFICATION AND STATISTICAL ANALYSIS
- DATA AND SOFTWARE AVAILABILITY

SUPPLEMENTAL INFORMATION

Supplemental Information includes six figures and six tables and can be found with this article online at <https://doi.org/10.1016/j.neuron.2018.09.026>.

ACKNOWLEDGMENTS

We thank Prof. Doug Black (UCLA) for the Rbfox1 monoclonal antibody (mAb) and Prof. Südhof (Stanford) for the Syt2 Ab. We thank the cores and shared resources of the NYULMC Division of Advanced Research Technologies and their personnel for their technical assistance: Mouse Genotyping Core (Jiali Deng and Jisen Dai); Cytometry and Cell Sorting Core (Kamilah Ryan, Keith Kobylarz, Yulia Chupalova, and Michael Gregory); Genome Technology Center (Yutong Zhang, Olga Aminova, and Adriana Heguy); and Applied Bioinformatics Laboratory (Aristotelis Tsirigos), which is supported in part by grant UL1 TR00038 from the National Center for Advancing Translational Sciences (NCATS). NIH. CCSC and GTC are supported by the Cancer Center Support Grant, P30CA016087, at the Laura and Isaac Perlmutter Cancer Center. We are grateful to Celine Vuong and Doug Black for their comments on the manuscript and to Chia-Ho Lin for her assistance with the iCLIP data analysis. Work in the G.F. lab is supported by the following NIH grants: R01 NS081297; R01 MH071679; R01 MH11529; and P01 NS074972 and by the Simons Foundation (SFARI grant 274578). Work in the B.R. lab is supported by NIH grants: R21NS108447 and P01 NS074972. X.H.J. was supported by EMBO (ALTF 303-2010), HFSP (LT000078/2011-L), the Bettencourt-Schueller Foundation, and by the NIH (K99 MH107684). B.W. was supported by a training grant (NIH, 5T32NS086750), and E.F. was supported by EMBO (ALTF 444-2018).

AUTHOR CONTRIBUTIONS

X.H.J., B.W., and G.F. conceived and developed the methodology and project. X.H.J., B.W., and N.Y. performed histology, behavior, imaging, and image analysis experiments. E.F. performed the molecular biology and biochemistry experiments. A.K.-J. and X.H.J. analyzed the RNA-seq experiments. G.Q. and M.J.N. performed the electrophysiological experiments. B.R. has provided guidance on the electrophysiological investigations. X.H.J., B.W., and E.F. analyzed and interpreted the results. X.H.J., B.W., E.F., and G.F. wrote the paper with review and editing provided by all authors. X.H.J., B.W., and G.F. performed project administration. X.H.J. and G.F. handled funding acquisition.

DECLARATION OF INTERESTS

The authors declare no competing interests.

Received: March 27, 2017

Revised: April 3, 2018

Accepted: September 14, 2018

Published: October 11, 2018

REFERENCES

- Abrahams, B.S., Arking, D.E., Campbell, D.B., Mefford, H.C., Morrow, E.M., Weiss, L.A., Menashe, I., Wadkins, T., Banerjee-Basu, S., and Packer, A. (2013). SFARI Gene 2.0: a community-driven knowledgebase for the autism spectrum disorders (ASDs). *Mol Autism* 4, 36.
- Allène, C., Cattani, A., Ackman, J.B., Bonifazi, P., Aniksztejn, L., Ben-Ari, Y., and Cossart, R. (2008). Sequential generation of two distinct synapse-driven network patterns in developing neocortex. *J. Neurosci.* 28, 12851–12863.
- Anders, S., Reyes, A., and Huber, W. (2012). Detecting differential usage of exons from RNA-seq data. *Genome Res.* 22, 2008–2017.
- Anders, S., Pyl, P.T., and Huber, W. (2015). HTSeq — a Python framework to work with high-throughput sequencing data. *Bioinformatics* 31, 166–169.
- Bandler, R.C., Mayer, C., and Fishell, G. (2017). Cortical interneuron specification: the juncture of genes, time and geometry. *Curr. Opin. Neurobiol.* 42, 17–24.
- Batista-Brito, R., and Fishell, G. (2009). *Current Topics in Developmental Biology* (Elsevier).
- Batista-Brito, R., Rossignol, E., Hjerling-Leffler, J., Denaxa, M., Wegner, M., Lefebvre, V., Pachnis, V., and Fishell, G. (2009). The cell-intrinsic requirement of Sox6 for cortical interneuron development. *Neuron* 63, 466–481.
- Benjamin, P.R., and Burke, J.F. (1994). Alternative mRNA splicing of the FMR1 gene and its role in neuropeptidergic signalling in a defined neural network. *Bioessays* 16, 335–342.
- Bhalla, K., Phillips, H.A., Crawford, J., McKenzie, O.L., Mulley, J.C., Eyre, H., Gardner, A.E., Kremmidoitis, G., and Callen, D.F. (2004). The de novo chromosome 16 translocations of two patients with abnormal phenotypes (mental retardation and epilepsy) disrupt the A2BP1 gene. *J. Hum. Genet.* 49, 308–311.
- Blackstad, T.W., and Flood, P.R. (1963). Ultrastructure of hippocampal axosomatic synapses. *Nature* 198, 542–543.
- Boyken, J., Grønborg, M., Riedel, D., Urlaub, H., Jahn, R., and Chua, J.J.E. (2013). Molecular profiling of synaptic vesicle docking sites reveals novel proteins but few differences between glutamatergic and GABAergic synapses. *Neuron* 78, 285–297.
- Buck, L.B., Bigelow, J.M., and Axel, R. (1987). Alternative splicing in individual Aplysia neurons generates neuropeptide diversity. *Cell* 51, 127–133.
- Close, J., Xu, H., De Marco García, N., Batista-Brito, R., Rossignol, E., Rudy, B., and Fishell, G. (2012). Satb1 is an activity-modulated transcription factor required for the terminal differentiation and connectivity of medial ganglionic eminence-derived cortical interneurons. *J. Neurosci.* 32, 17690–17705.
- Damianov, A., Ying, Y., Lin, C.-H., Lee, J.-A., Tran, D., Vashisht, A.A., Bahrami-Samani, E., Xing, Y., Martin, K.C., Wohlschlegel, J.A., and Black, D.L. (2016). Rbfox proteins regulate splicing as part of a large multiprotein complex LASR. *Cell* 165, 606–619.
- Dillman, A.A., Hauser, D.N., Gibbs, J.R., Nalls, M.A., McCoy, M.K., Rudenko, I.N., Galter, D., and Cookson, M.R. (2013). mRNA expression, splicing and editing in the embryonic and adult mouse cerebral cortex. *Nat. Neurosci.* 16, 499–506.
- Dobin, A., Davis, C.A., Schlesinger, F., Drenkow, J., Zaleski, C., Jha, S., Batut, P., Chaisson, M., and Gingeras, T.R. (2013). STAR: ultrafast universal RNA-seq aligner. *Bioinformatics* 29, 15–21.
- Fogarty, M., Grist, M., Gelman, D., Marín, O., Pachnis, V., and Kessaris, N. (2007). Spatial genetic patterning of the embryonic neuroepithelium generates GABAergic interneuron diversity in the adult cortex. *J. Neurosci.* 27, 10935–10946.
- Fogel, B.L., Wexler, E., Wahnich, A., Friedrich, T., Vijayendran, C., Gao, F., Parikshak, N., Konopka, G., and Geschwind, D.H. (2012). RBFOX1 regulates both splicing and transcriptional networks in human neuronal development. *Hum. Mol. Genet.* 21, 4171–4186.
- Fuccillo, M.V., Földy, C., Gökcce, Ö., Rothwell, P.E., Sun, G.L., Malenka, R.C., and Südhof, T.C. (2015). Single-cell mRNA profiling reveals cell-type-specific expression of neuroligin isoforms. *Neuron* 87, 326–340.
- Gehman, L.T., Stoilov, P., Maguire, J., Damianov, A., Lin, C.-H., Shiue, L., Ares, M., Jr., Mody, I., and Black, D.L. (2011). The splicing regulator Rbfox1 (A2BP1) controls neuronal excitation in the mammalian brain. *Nat. Genet.* 43, 706–711.
- Gong, S., Zheng, C., Doughty, M.L., Losos, K., Didkovsky, N., Schambra, U.B., Nowak, N.J., Joyner, A., Leblanc, G., Hatten, M.E., and Heintz, N. (2003). A gene expression atlas of the central nervous system based on bacterial artificial chromosomes. *Nature* 425, 917–925.
- Han, A., Stoilov, P., Linares, A.J., Zhou, Y., Fu, X.D., and Black, D.L. (2014). De novo prediction of PTBP1 binding and splicing targets reveals unexpected features of its RNA recognition and function. *PLoS Comput. Biol.* 10, e1003442.
- Harris, J.A., Hirokawa, K.E., Sorensen, S.A., Gu, H., Mills, M., Ng, L.L., Bohn, P., Mortrud, M., Ouellette, B., Kidney, J., et al. (2014). Anatomical characterization of Cre driver mice for neural circuit mapping and manipulation. *Front. Neural Circuits* 8, 76.
- Heintz, N. (2004). Gene expression nervous system atlas (GENSAT). *Nat. Neurosci.* 7, 483.
- Hempel, C.M., Sugino, K., and Nelson, S.B. (2007). A manual method for the purification of fluorescently labeled neurons from the mammalian brain. *Nat. Protoc.* 2, 2924–2929.

- Huang, W., Sherman, B.T., and Lempicki, R.A. (2009). Systematic and integrative analysis of large gene lists using DAVID bioinformatics resources. *Nat. Protoc.* 4, 44–57.
- Iijima, T., Wu, K., Witte, H., Hanno-Iijima, Y., Glatter, T., Richard, S., and Scheiffele, P. (2011). SAM68 regulates neuronal activity-dependent alternative splicing of neuroligin-1. *Cell* 147, 1601–1614.
- Ippolito, D.M., and Eroglu, C. (2010). Quantifying synapses: an immunocytochemistry-based assay to quantify synapse number. *J. Vis. Exp.* 45, 2270.
- Jin, Y., Suzuki, H., Maegawa, S., Endo, H., Sugano, S., Hashimoto, K., Yasuda, K., and Inoue, K. (2003). A vertebrate RNA-binding protein Fox-1 regulates tissue-specific splicing via the pentanucleotide GCAUG. *EMBO J.* 22, 905–912.
- Johnson, M.B., Kawasawa, Y.I., Mason, C.E., Kruskal, Z., Coppola, G., Bogdanović, D., Geschwind, D.H., Mane, S.M., State, M.W., and Sestan, N. (2009). Functional and evolutionary insights into human brain development through global transcriptome analysis. *Neuron* 62, 494–509.
- Kent, W.J., Zweig, A.S., Barber, G., Hinrichs, A.S., and Karolchik, D. (2010). BigWig and BigBed: enabling browsing of large distributed datasets. *Bioinformatics* 26, 2204–2207.
- Lee, J.A., Tang, Z.Z., and Black, D.L. (2009). An inducible change in Fox-1/A2BP1 splicing modulates the alternative splicing of downstream neuronal target exons. *Genes Dev.* 23, 2284–2293.
- Lee, J.-A., Damianov, A., Lin, C.-H., Fontes, M., Parikshak, N.N., Anderson, E.S., Geschwind, D.H., Black, D.L., and Martin, K.C. (2016). Cytoplasmic Rbfox1 regulates the expression of synaptic and autism-related genes. *Neuron* 89, 113–128.
- Li, L., Tasic, B., Micheva, K.D., Ivanov, V.M., Spletter, M.L., Smith, S.J., and Luo, L. (2010). Visualizing the distribution of synapses from individual neurons in the mouse brain. *PLoS ONE* 5, e11503.
- Linares, A.J., Lin, C.H., Damianov, A., Adams, K.L., Novitsch, B.G., and Black, D.L. (2015). The splicing regulator PTBP1 controls the activity of the transcription factor Pbx1 during neuronal differentiation. *eLife* 4, e09268.
- Lodato, S., Tomassy, G.S., De Leonibus, E., Uzcatagui, Y.G., Andolfi, G., Armentano, M., Touzot, A., Gaztelu, J.M., Arlotta, P., Menendez de la Prida, L., and Studer, M. (2011). Loss of COUP-TFI alters the balance between caudal ganglionic eminence- and medial ganglionic eminence-derived cortical interneurons and results in resistance to epilepsy. *J. Neurosci.* 31, 4650–4662.
- Lovci, M.T., Ghanem, D., Marr, H., Arnold, J., Gee, S., Parra, M., Liang, T.Y., Stark, T.J., Gehman, L.T., Hoon, S., et al. (2013). Rbfox proteins regulate alternative mRNA splicing through evolutionarily conserved RNA bridges. *Nat. Struct. Mol. Biol.* 20, 1434–1442.
- Love, M.I., Huber, W., and Anders, S. (2014). Moderated estimation of fold change and dispersion for RNA-seq data with DESeq2. *Genome Biol.* 15, 550.
- Maniatis, T., and Tasic, B. (2002). Alternative pre-mRNA splicing and proteome expansion in metazoans. *Nature* 418, 236–243.
- Marin, O. (2012). Interneuron dysfunction in psychiatric disorders. *Nat. Rev. Neurosci.* 13, 107–120.
- Martin, C.L., Duvall, J.A., Ilkin, Y., Simon, J.S., Arreaza, M.G., Wilkes, K., Alvarez-Retuerto, A., Whicello, A., Powell, C.M., Rao, K., et al. (2007). Cytogenetic and molecular characterization of A2BP1/FOX1 as a candidate gene for autism. *Am. J. Med. Genet. B. Neuropsychiatr. Genet.* 144B, 869–876.
- Mayer, C., Hafemeister, C., Bandler, R.C., Machold, R., Batista Brito, R., Jaglin, X., Allaway, K., Butler, A., Fishell, G., and Satija, R. (2018). Developmental diversification of cortical inhibitory interneurons. *Nature* 555, 457–462.
- Mi, D., Li, Z., Lim, L., Li, M., Moissidis, M., Yang, Y., Gao, T., Hu, T.X., Pratt, T., Price, D.J., et al. (2018). Early emergence of cortical interneuron diversity in the mouse embryo. *Science* 360, 81–85.
- Minlebaev, M., Colonnese, M., Tsintsadze, T., Sirota, A., and Khazipov, R. (2011). Early γ oscillations synchronize developing thalamus and cortex. *Science* 334, 226–229.
- Miyoshi, G., Hjerling-Leffler, J., Karayannis, T., Sousa, V.H., Butt, S.J.B., Battiste, J., Johnson, J.E., Machold, R.P., and Fishell, G. (2010). Genetic fate mapping reveals that the caudal ganglionic eminence produces a large and diverse population of superficial cortical interneurons. *J. Neurosci.* 30, 1582–1594.
- Nakahata, S., and Kawamoto, S. (2005). Tissue-dependent isoforms of mammalian Fox-1 homologs are associated with tissue-specific splicing activities. *Nucleic Acids Res.* 33, 2078–2089.
- Nguyen, T.M., Schreiner, D., Xiao, L., Trauttmüller, L., Bornmann, C., and Scheiffele, P. (2016). An alternative splicing switch shapes neuroligin repertoires in principal neurons versus interneurons in the mouse hippocampus. *eLife* 5, e22757.
- Norris, A.D., Gao, S., Norris, M.L., Ray, D., Ramani, A.K., Fraser, A.G., Morris, Q., Hughes, T.R., Zhen, M., and Calarco, J.A. (2014). A pair of RNA-binding proteins controls networks of splicing events contributing to specialization of neural cell types. *Mol. Cell* 54, 946–959.
- Nowakowski, T.J., Bhaduri, A., Pollen, A.A., Alvarado, B., Mostajo-Radji, M.A., Di Lullo, E., Haeussler, M., Sandoval-Espinosa, C., Liu, S.J., Velmeshev, D., et al. (2017). Spatiotemporal gene expression trajectories reveal developmental hierarchies of the human cortex. *Science* 358, 1318–1323.
- Pan, Q., Shai, O., Lee, L.J., Frey, B.J., and Blencowe, B.J. (2008). Deep surveying of alternative splicing complexity in the human transcriptome by high-throughput sequencing. *Nat. Genet.* 40, 1413–1415.
- Parikshak, N.N., Swarup, V., Belgard, T.G., Irimia, M., Ramaswami, G., Gandal, M.J., Hartl, C., Leppä, V., Ubieta, L.T., Huang, J., et al. (2016). Genome-wide changes in lncRNA, splicing, and regional gene expression patterns in autism. *Nature* 540, 423–427.
- Park, J.W., Jung, S., Rouchka, E.C., Tseng, Y.T., and Xing, Y. (2016). rMAPS: RNA map analysis and plotting server for alternative exon regulation. *Nucleic Acids Res.* 44 (W1), W333–W338.
- Priya, R., Paredes, M.F., Karayannis, T., Yusuf, N., Liu, X., Jaglin, X., Graef, I., Alvarez-Buylla, A., and Fishell, G. (2018). Activity Regulates Cell Death within Cortical Interneurons through a Calcineurin-Dependent Mechanism. *Cell Rep.* 22, 1695–1709.
- Quinlan, A.R., and Hall, I.M. (2010). BEDTools: a flexible suite of utilities for comparing genomic features. *Bioinformatics* 26, 841–842.
- Racine, R.J. (1972). Modification of seizure activity by electrical stimulation. II. Motor seizure. *Electroencephalogr. Clin. Neurophysiol.* 32, 281–294.
- Raj, B., and Blencowe, B.J. (2015). Alternative splicing in the mammalian nervous system: recent insights into mechanisms and functional roles. *Neuron* 87, 14–27.
- Sebat, J., Lakshmi, B., Malhotra, D., Troge, J., Lese-Martin, C., Walsh, T., Yamrom, B., Yoon, S., Krasnitz, A., Kendall, J., et al. (2007). Strong association of de novo copy number mutations with autism. *Science* 316, 445–449.
- Shen, S., Park, J.W., Lu, Z.-X., Lin, L., Henry, M.D., Wu, Y.N., Zhou, Q., and Xing, Y. (2014). rMATS: robust and flexible detection of differential alternative splicing from replicate RNA-seq data. *Proc. Natl. Acad. Sci. USA* 111, E5593–E5601.
- Sousa, V.H., Miyoshi, G., Hjerling-Leffler, J., Karayannis, T., and Fishell, G. (2009). Characterization of Nkx6-2-derived neocortical interneuron lineages. *Cereb. Cortex* 19 (Suppl 1), i1–i10.
- Sommeijer, J.P., and Levelt, C.N. (2012). Synaptotagmin-2 is a reliable marker for parvalbumin positive inhibitory boutons in the mouse visual cortex. *PLoS ONE* 7, e35323.
- Sommer, B., Keinänen, K., Verdoorn, T.A., Wisden, W., Burnashev, N., Herb, A., Köhler, M., Takagi, T., Sakmann, B., and Seeburg, P.H. (1990). Flip and flop: a cell-specific functional switch in glutamate-operated channels of the CNS. *Science* 249, 1580–1585.
- Taniguchi, H., He, M., Wu, P., Kim, S., Paik, R., Sugino, K., Kvitsiani, D., Fu, Y., Lu, J., Lin, Y., et al. (2011). A resource of Cre driver lines for genetic targeting of GABAergic neurons in cerebral cortex. *Neuron* 71, 995–1013.
- Tasic, B., Menon, V., Nguyen, T.N., Kim, T.-K., Jarsky, T., Yao, Z., Levi, B., Gray, L.T., Sorensen, S.A., Dolbeare, T., et al. (2016). Adult mouse cortical cell taxonomy revealed by single cell transcriptomics. *Nat. Neurosci.* 19, 335–346.

- Tasic, B., Yao, Z., Smith, K.A., Graybiel, L., Nguyen, T.N., Bertagnolli, D., Goldy, J., Garren, E., Economou, M.N., Viswanathan, S., et al. (2017). Shared and distinct transcriptomic cell types across neocortical areas. *bioRxiv*. <https://doi.org/10.1101/229542>.
- Trapnell, C., Hendrickson, D.G., Sauvageau, M., Goff, L., Rinn, J.L., and Pachter, L. (2013). Differential analysis of gene regulation at transcript resolution with RNA-seq. *Nat. Biotechnol.* **31**, 46–53.
- Tremblay, R., Lee, S., and Rudy, B. (2016). GABAergic interneurons in the neocortex: from cellular properties to circuits. *Neuron* **91**, 260–292.
- Underwood, J.G., Boutz, P.L., Dougherty, J.D., Stoilov, P., and Black, D.L. (2005). Homologues of the *Caenorhabditis elegans* Fox-1 protein are neuronal splicing regulators in mammals. *Mol. Cell Biol.* **25**, 10005–10016.
- Voineagu, I., Wang, X., Johnston, P., Lowe, J.K., Tian, Y., Horvath, S., Mill, J., Cantor, R.M., Blencowe, B.J., and Geschwind, D.H. (2011). Transcriptomic analysis of autistic brain reveals convergent molecular pathology. *Nature* **474**, 380–384.
- Vuong, C.K., Black, D.L., and Zheng, S. (2016). The neurogenetics of alternative splicing. *Nat. Rev. Neurosci.* **17**, 265–281.
- Vuong, C.K., Wei, W., Lee, J.A., Lin, C.H., Damianov, A., de la Torre-Ubieta, L., Halabi, R., Otis, K.O., Martin, K.C., O'Dell, T.J., and Black, D.L. (2018). Rbfox1 regulates synaptic transmission through the inhibitory neuron-specific vSNARE Vamp1. *Neuron* **98**, 127–141.e7.
- Wamsley, B., and Fishell, G. (2017). Genetic and activity-dependent mechanisms underlying interneuron diversity. *Nat. Rev. Neurosci.* **18**, 299–309.
- Wang, E.T., Sandberg, R., Luo, S., Khrebtkova, I., Zhang, L., Mayr, C., Kingsmore, S.F., Schroth, G.P., and Burge, C.B. (2008). Alternative isoform regulation in human tissue transcriptomes. *Nature* **456**, 470–476.
- Weyn-Vanhenryck, S.M., Mele, A., Yan, Q., Sun, S., Farny, N., Zhang, Z., Xue, C., Herre, M., Silver, P.A., Zhang, M.Q., et al. (2014). HITS-CLIP and integrative modeling define the Rbfox splicing-regulatory network linked to brain development and autism. *Cell Rep.* **6**, 1139–1152.
- Yan, Q., Weyn-Vanhenryck, S.M., Wu, J., Sloan, S.A., Zhang, Y., Chen, K., Wu, J.Q., Barres, B.A., and Zhang, C. (2015). Systematic discovery of regulated and conserved alternative exons in the mammalian brain reveals NMD modulating chromatin regulators. *Proc. Natl. Acad. Sci. USA* **112**, 3445–3450.
- Yang, J.-W., Hanganu-Opatz, I.L., Sun, J.-J., and Luhmann, H.J. (2009). Three patterns of oscillatory activity differentially synchronize developing neocortical networks in vivo. *J. Neurosci.* **29**, 9011–9025.
- Yang, J.W., An, S., Sun, J.J., Reyes-Puerta, V., Kindler, J., Berger, T., Kilb, W., and Luhmann, H.J. (2013). Thalamic network oscillations synchronize ontogenetic columns in the newborn rat barrel cortex. *Cereb. Cortex* **23**, 1299–1316.
- Yu, M., Xi, Y., Pollack, J., Debais-Thibaud, M., Macdonald, R.B., and Ekker, M. (2011). Activity of *dlx5a/dlx6a* regulatory elements during zebrafish GABAergic neuron development. *Int. J. Dev. Neurosci.* **29**, 681–691.
- Yu, G., Wang, L.-G., and He, Q.-Y. (2015). ChIPseeker: an R/Bioconductor package for ChIP peak annotation, comparison and visualization. *Bioinformatics* **31**, 2382–2383.
- Zeisel, A., Muñoz-Manchado, A.B., Codeluppi, S., Lönnerberg, P., La Manno, G., Jureus, A., Marques, S., Munguba, H., He, L., Betsholtz, C., et al. (2015). Brain structure. Cell types in the mouse cortex and hippocampus revealed by single-cell RNA-seq. *Science* **347**, 1138–1142.
- Zhang, Y., Liu, T., Meyer, C.A., Eeckhoutte, J., Johnson, D.S., Bernstein, B.E., Nusbaum, C., Myers, R.M., Brown, M., Li, W., and Liu, X.S. (2008). Model-based analysis of ChIP-seq (MACS). *Genome Biol.* **9**, R137.
- Zhang, Y., Chen, K., Sloan, S.A., Bennett, M.L., Scholze, A.R., O'Keefe, S., Phatnani, H.P., Guarnieri, P., Caneda, C., Ruderisch, N., et al. (2014). An RNA-sequencing transcriptome and splicing database of glia, neurons, and vascular cells of the cerebral cortex. *J. Neurosci.* **34**, 11929–11947.
- Zhang, X., Chen, M.H., Wu, X., Kodani, A., Fan, J., Doan, R., Ozawa, M., Ma, J., Yoshida, N., Reiter, J.F., et al. (2016). Cell-type-specific alternative splicing governs cell fate in the developing cerebral cortex. *Cell* **166**, 1147–1162.e15.

STAR★METHODS

KEY RESOURCES TABLE

REAGENT or RESOURCE	SOURCE	IDENTIFIER
Antibodies		
Anti-GFP, Chicken Polyclonal IgY (1:1000)	Abcam	Ab13970, RRID: AB_10561923
Anti-RFP(5F8), Rat Monoclonal	ChromoTek	5f8-100, RRID: AB_2336064
Living Colors Anti-DsRed(RFP), Rabbit Polyclonal	Clontech	632496, RRID: AB_10013483
Anti-Somatostatin (YC7), Rat Monoclonal IgG2b	EMD Millipore	MAB354, RRID: AB_2255365
Somatostatin 14-Undiluted antiserum for IHC, Host: Rabbit	Peninsula Laboratories	T-4103.0050, RRID: AB_518614
Anti-Parvalbumin (PV) Goat	Swant	PVG 213, RRID: AB_2721207
Anti-Parvalbumin (PV) Rabbit	Swant	PV25, RRID: AB_10000344
Anti-Vasoactive Intestinal Peptide (VIP) (Rabbit 1:1000)	ImmunoStar	20077, RRID: AB_572270
Wisteria Floribundas (WFA)	Sigma	L1516-2mg, RRID: AB_2620171
Anti-cFos (4) Antibody sc-52	Santa Cruz Biotechnology	Sc-166940, RRID: AB_10609634
Rbfox(1D10)	Gift from Dr. Douglas Black; Lee et al., 2009	RRID: AB_2737389
Anti-VGAT, Rabbit Polyclonal, Cytoplasmic Domain	Synaptic Systems	131 003, RRID: AB_887869
Anti- β -Actin–Peroxidase	Sigma	A3854, RRID: AB_262011
Anti-Gephyrin	Synaptic Systems	147011, RRID: AB_2232546
Anti-Fox1, clone 1D10	Millipore	MABE985, RRID: AB_2737389
Synaptotagmin-2	Gift from Dr. Thomas Südhof; Sommeijer and Levitt, 2012	N/A
Critical Commercial Assays		
Papain Disassociation System	Worthington	LK003150
Pronase	Sigma	10165921001
DNase I Recombinant, RNase-free	Roche	04716728001
PicoPure RNA Isolation Kit	Applied Biosystems	KIT0204
Bioanalyzer RNA Analysis Kit	Agilent	5067-1511
Bionalyzer High Sensitivity DNA Analysis Kit	Agilent	5067-4626
Kainic Acid Monohydrate	Sigma-Aldrich	K0250
Superscript II Reverse Transcriptase	Invitrogen	18064-014
SYBR select master mix	Applied Biosystems	4472908
Trizol LS Reagent	Ambion	10296-010
Purelink DNase Set	Ambion	12185010
Ovation RNA-Seq System V2	NuGEN	7102-32
Kapa LTP library preparation kit for Illumina platforms	Kapa Biosystems	KK8232
Agencourt RNA Clean XP	Beckman Coulter	A63987
Agencourt AMPure XP beads	Beckman Coulter	514103
Magna RIP	Millipore	17-700
Deposited Data		
Raw and analyzed data	This paper	GEO: GSE119998
Experimental Models: Organisms/Strains		
Dlx6aCre	The Jackson Laboratory	Stock # 008199
SSTcre	The Jackson Laboratory	Stock # 013044
Tac1Cre	The Jackson Laboratory	Stock # 021877
Ai9	The Jackson Laboratory	Stock # 007909
RCE LoxP	Miyoshi et al., 2010	N/A
Ai65	The Jackson Laboratory	Stock # 021875

(Continued on next page)

Continued

REAGENT or RESOURCE	SOURCE	IDENTIFIER
Rosa-tTa	Gift from Martyn Goulding	N/A
TetO-SyepGFP	The Jackson Laboratory	Stock # 012345
Ai32	The Jackson Laboratory	Stock # 012569
Lhx6eGFP	GENSAT	MMRRC 000246-MU
GIN	The Jackson Laboratory	Stock # 003718
Dlx5/6FlpE	Fogarty et al., 2007	N/A
Rbfox1	The Jackson Laboratory	Stock # 014089
Oligonucleotides		
Primers for RT-PCR	This paper	STAR Methods
Software and Algorithms		
STAR aligner (v.2.5.0c)	Dobin et al., 2013	N/A
Picard tools (v.1.126)	Broad Institute	http://broadinstitute.github.io/picard/
BEDTools (v.2.17.0)	Quinlan and Hall, 2010	N/A
bedGraphToBigWig (v.4)	Kent et al., 2010	N/A
HTSeq (v.0.6.0)	Anders et al., 2015	N/A
DESeq2 (v.3.0)	Love et al., 2014	N/A
Cufflinks (v.2.0)	Trapnell et al., 2013	N/A
DEXSeq (v.3.1)	Anders et al., 2012	N/A
rMATS (v.3.0.9)	Shen et al., 2014	N/A
Prism7.0b	GraphPad	N/A
MACS (v.1.4.2)	Zhang et al., 2008	N/A
ChIPseeker (v.1.8.0)	Yu et al., 2015	N/A
R (v.3.1.1)	The R Foundation	https://www.r-project.org/

CONTACT FOR REAGENT AND RESOURCE SHARING

Further information and requests for resources and reagents should be directed to and will be fulfilled by the Lead Contact Gordon Fishell (gordon_fishell@hms.harvard.edu).

EXPERIMENTAL MODEL AND SUBJECT DETAILS**Mouse Maintenance and Mouse Strains**

All experimental procedures were conducted in accordance with the National Institutes of Health guidelines and were approved by the Institutional Animal Care and Use Committee of the NYU School of Medicine. Generation and genotyping of *Dlx6a*^{Cre} (Yu et al., 2011), *SST*^{Cre} (Taniguchi et al., 2011), *Tac1-IRES2-Cre* (referred to as *Tac1*^{Cre}) (Harris et al., 2014), *RCE*^{eGFP} (Sousa et al., 2009), *Lhx6* BAC transgenic (referred to as *Lhx6::eGFP*) (Gong et al., 2003; Heintz, 2004), *Rbfox1*^{LoxP/LoxP} (Gehman et al., 2011), TRE-Bi-SypGFP-TdTomato (Li et al., 2010) and *Ai9*^{LoxP/LoxP}, *Ai32*^{LoxP/LoxP}, *Rosa-tTa*^{LoxP/LoxP}. All mouse strains were maintained on a mixed background (Swiss Webster and C57/ B16). The day of plug is considered as E0.5, the day of birth is considered P0. Information about the mouse strains including genotyping protocols can be found at <https://www.jax.org/> and elsewhere (see above references).

METHOD DETAILS**Immunocytochemistry and Imaging**

Embryos, neonate, juvenile, and adult mice were perfused inter cardiac with 4% PFA after being anesthetized either on ice or using Sleepaway IP administration. Brains that were processed for free-floating immunofluorescence were first post-fixed in 4% PFA overnight at 4°C. Brains were sectioned on a Leica vibratome at 50 μm-thickness and stored in a cryoprotecting solution (40% PBS, 30% glycerol and 30% ethylene glycol) at -20°C until use. For immunofluorescence, floating sections were placed in 2 mL tubes for >30 min at RT in PBS, then blocked for >1 hr at RT in blocking buffer and incubated for 2-3 days at 4°C with primary antibodies in blocking buffer. Sections were washed 3 × 30 min at RT in PBS, incubated overnight at 4°C with secondary antibodies and DAPI in blocking buffer, washed 3 × 30 min at RT in PBST and once with PBS before being mounted on glass slides.

Brains that were processed for immunofluorescence on slides were post-fixed and cryopreserved following the perfusion and brain harvest. 16 μm coronal sections were obtained using Cryostat (Leica Biosystems) and collected on super-frost coated slides, then allowed to dry and stored at -20°C until use. For immunofluorescence, cryosections were thawed and allowed to dry for 5–10 min and rinsed twice in 1x PBS.

They were incubated at room temperature in a blocking solution of PBST (PBS-0.1%Tx-100) and 10% normal donkey serum (NDS) for 60min, followed by incubation with primary antibodies in PBS-T and 1% NDS at 4°C overnight. Samples were then washed 3 times with PBS-T and incubated with fluorescence conjugated secondary Alexa antibodies (Life Technologies) in PBS-T with 1% NDS at room temperature for 60–90min. Slides were then incubated for 30 s with DAPI, washed 3 times with PBS-T and once with PBS. Finally, slides were mounted with Fluoromount G (Southern Biotech) and imaged. Primary antibodies are listed in [Key Resources Table](#).

Confocal Imaging and Synaptic Puncta Analysis

Animals were perfused as described above. Post-fixation incubation prior to cryopreservation was skipped. Cryostat sections (16 μm) were subjected to immunohistochemistry as described above. Images were taken within the somatosensory cortex of at least three different sections from three different animals per genotype with a Zeiss LSM 510 and 800 laser scanning confocal microscope. Scans were performed to obtain 4 optical Z sections of 0.33 μm each (totaling ~ 1.2 μm max projection) with a 63x/1.4 Oil DIC objective. The same scanning parameters (i.e., pinhole diameter, laser power/offset, speed/averaging) were used for all images. Maximum projections of 4 consecutive 0.33 μm stacks were analyzed with ImageJ (NIH) puncta analyzer plugin ([Ippolito and Eroglu, 2010](#)) to count the number of individual puncta consisting of pre-synaptic and post-synaptic markers that are close enough together to be considered a putative synaptic puncta. Synaptic puncta density per image was calculated by normalization to total puncta acquired for each individual channel accounted in each image for each condition. Puncta Analyzer plugin is written by Barry Wark, and is available for download (<https://github.com/physion/puncta-analyzer>).

Seizure Susceptibility

We investigated the seizure susceptibility according to a modified Racine Scale ([Gehman et al., 2011](#); [Racine, 1972](#)). Stage 0, normal behavior; stage 1, immobility; stage 2, mouth and facial movements; stage 3, head bobbing; stage 4, forelimb clonus; stage 5, rearing; stage 6, continuous rearing and falling (tonic-clonic seizures); and stage 7, status epilepticus and/or death. For each animal (aged P12–P14), the score was determined every 5 min for up to 70 mins from time of kainic acid (12mg/kg) intra-peritoneal injection. We used the maximum score of each animal's behavior at each 5 min interval to determine the average score and standard deviation for both control (*Dlx6a^{Cre};Rbfox1^{+/+};RCE^{eGFP}*) (N = 5) and *Dlx-cKO* (*Dlx6a^{Cre};Rbfox1^{F/F};RCE^{eGFP}*) (N = 9).

Electrophysiological Recordings

Slice preparation: Acute brain slices (300 μm thick) were prepared from P17–P60 mice. Mice were deeply anesthetized with euthasol and decapitated. The brain was removed and placed in ice-cold modified artificial cerebrospinal fluid (ACSF) of the following composition (in mM): 87 NaCl, 26 NaHCO_3 , 2.5 KCl, 1.25 NaH_2PO_4 , 0.5 CaCl₂, 7 MgCl₂, 10 glucose, 75 sucrose saturated with 95% O₂, 5% CO₂ at pH = 7.4. Coronal sections were cut using a vibrating microtome (Leica, VT 1200S). Slices were then incubated at $34\text{--}35^{\circ}\text{C}$ for 30 min and then stored at room temperature until use.

Recordings: Slices were transferred to the recording chamber of an up-right microscope (Olympus BX51) equipped with oblique illumination Olympus optics (Olympus) and an infrared camera system (Q-Imaging). Cells were visualized using a 40 or 60X IR water immersion objective. Slices were superfused with preheated ACSF of the following composition (in mM): 124 NaCl, 26 NaHCO_3 , 3 KCl, 1.25 NaH_2PO_4 , 1.6 CaCl₂, 2 MgCl₂, 10 glucose, saturated with 95% O₂, 5% CO₂ at pH = 7.4 and maintained at a constant temperature ($31\text{--}33^{\circ}\text{C}$). Whole-cell recordings were made from randomly selected tdTomato-positive interneurons or tdTomato-negative pyramidal cells from layer II–III of the somatosensory cortex. Recording pipettes were pulled from borosilicate glass capillaries (Harvard Apparatus) and had a resistance of 3–5 M Ω when filled with the appropriate internal solution, as reported below. Recordings were performed using a Multiclamp 700B amplifier (Molecular Devices). The current clamp signals were filtered at 10 kHz and digitized at 40 kHz using a Digidata 1550A and the Clampex 10 program suite (Molecular Devices). Miniature synaptic currents were filtered at 3 kHz and recorded with a sampling rate of 10 kHz. Voltage-clamp recordings were performed at a holding potential of 0 mV after application of kynurenic acid (3 mM), for current-clamp recordings performed at a holding potential of -65 mV after application of a combination of CNQX (10 μM) and D-AP5 (25 μM). Cells were only accepted for analysis if the initial series resistance was less than 40 M Ω and did not change by more than 20% throughout the recording period. The series resistance was compensated online by at least $\sim 60\%$ in voltage-clamp mode. No correction was made for the junction potential between the pipette and the ACSF.

Passive and active membrane properties were recorded in current clamp mode by applying a series of hyperpolarizing and depolarizing current steps and the analysis was done in Clampfit (Molecular Devices). The highest firing frequency was calculated from a series of 20 pA depolarizing 1 s long current steps (range 0–520 pA). The cell input resistance was calculated from the peak of the voltage response to a 50 pA hyperpolarizing 1 s long current step according to Ohm's law. Analysis of the action potential properties was done on the first spike observed during a series of depolarizing steps. Threshold was defined as the voltage at the point when the slope first exceeds a value of 20 $\text{V}\cdot\text{s}^{-1}$. Rheobase was defined as the amplitude of the first depolarizing step at which firing was observed. Analysis of miniature inhibitory events was done using Clampfit template search. All values presented in the manuscript

are average \pm standard error of the mean (SEM) and all the statistical values are obtained doing a standard Student's *t* test, unless otherwise stated (**p* \leq 0.05, ***p* \leq 0.01, ****p* \leq 0.005).

Pipette solutions: Solution for voltage-clamp recordings from pyramidal cells (in mM): 130 Cs-methanesulfonate, 5 CsCl, 1 HEPES, 0.2 EGTA, 4 MgATP, 0.3 Na-GTP, 5 Phosphocreatine-Tris, 5 QX-314-Cl and 0.3%–0.5% biocytin, equilibrated with KOH a pH = 7.3. Solution for current clamp recordings from interneurons (in mM): 130 K-Gluconate, 10 KCl, 10 HEPES, 0.2 EGTA, 4 MgATP, 0.3 NaGTP, 5 Phosphocreatine and 0.3%–0.5% biocytin, equilibrated with KOH CO₂ to a pH = 7.3.

Optogenetic Stimulation

Blue-light (470 nm) was transmitted to the slice from an LED placed under the condenser of an up-right microscope (Olympus BX50). IPSCs were elicited by applying single 1 ms blue-light pulses of varying intensities (max. stimulation intensity \sim 0.33 mW/mm²) and directed to layer II–III of the slice in the recording chamber. Light pulses were delivered every 5 s increasing the light intensity. The LED output was driven by a TTL output from the Clampex software of the pCLAMP 9.0 program suite (Molecular Devices).

Isolation of Cortical Interneurons from the Developing Mouse Cerebral Cortex

Cortical interneurons were dissociated from embryonic cortices (E18.5) using the Worthington papain dissociation kit and in accordance with the manufacturer's guidelines, except for the concentration of papain used during the tissue digestion (9U/mL).

Cortical interneurons were dissociated from postnatal mouse cortices (P4, P8, P12, P22) as described (Hempel et al., 2007). We collected at least 3–7 cKO and 3–5 wt brains, and maintained overall balanced numbers of females and males within each condition, in order to avoid sex-related gene expression biases. Following dissociation, cortical neurons in suspension were filtered and GFP+ or TdTomato+ fate-mapped interneurons were sorted by fluorescence activated-cell sorting on either a Beckman Coulter MoFlo (Cytomation), BD FACSAria II SORP or Sony SY3200. Sorted cINs are collected and lysed in 500 μ l TRIzol LS Reagent, then thoroughly mixed and stored at -80° C until further totRNA extraction.

Nucleic Acid Extraction, RNA Amplification, cDNA Library Preparation, and RNA Sequencing

Total RNAs from sorted cINs (E18.5–P22 mouse cortices for Figure 1 and P8 mouse cortices for Figures 6 and S6) were extracted using TRIzol LS Reagent and PicoPure columns (if less than 20K cells were recovered) or PureLink RNA Mini Kit (if more than 20K cells were recovered), with PureLink DNase for on-column treatment, following the manufacturers' guidelines. RNA quality and quantity were measured with a Picochip using an Agilent Bioanalyzer and only samples with high quality total RNA were used (RIN: 7.5–10.0). 20ng of total RNA was used for cDNA synthesis and amplification, using NuGEN Ovation RNA-Seq System V2 kit (NuGEN part # 7102). 100 ng of amplified cDNA were used to make a library using the Ovation Ultralow Library System (NuGEN part # 0330). 10 cycles of PCR were run during the amplification step. The samples were pooled and run as 50-nucleotide paired-end read rapid with the Illumina HiSeq 2500 sequencer (v4 chemistry), to generate >50 million reads per sample. Library preparation, quantification, pooling, clustering, and sequencing was carried out at the NYULMC Genome Technology Center. qRT-PCR (quantitative RT-PCR) was performed using SYBR select master mix (Thermo-Fisher Scientific) on cDNA synthesized using SuperScript II reverse transcriptase and oligo(dT) primers.

List of RT- and qRT-PCR primers:

Primer name	Orientation	Sequence	Target
MmPpia_F	Forward	AGGGTGGTGACTTTACACGC	Housekeeping gene <i>Ppia</i>
MmPpia_R	Reverse	TGCCTTCTTTCACCTTCCCA	Housekeeping gene <i>Ppia</i>
MmRbfox1_F1	Forward	CGGTGTTGTTTACCAGGATGG	<i>Rbfox1</i> Exon 15–16 junction
MmRbfox1_Ra	Reverse	TAAACTCGTCCGTAACGTGCAC	<i>Rbfox1</i> Exon 18–20 junction
MmRbfox1_Ri	Reverse	GTGTTACAAGAAATTCATCTGTTGC	<i>Rbfox1</i> Exon 19
5'-6FAM	Forward	6FAM-CGTCGCCGTCCAGCTCGACCAG	Fluorescently-labeled primer
Jakmip3_Fw	Forward	CGTCGCCGTCCAGCTCGACCAGGGAGTGTCTACCATCTGCATCA	<i>Jakmip3</i> Exon 3
Jakmip3_Rv	Reverse	AGCTTACGGATGATGGCACT	<i>Jakmip3</i> Exon 5
Lrrcc1_Fw	Forward	CGTCGCCGTCCAGCTCGACCAGGACACCTGAGAACCCTGGAA	<i>Lrrcc1</i> Exon 2
Lrrcc1_Rv	Reverse	TTCGTTCTTCTTTGCATAATCG	<i>Lrrcc1</i> Exon 4
Mtmr14_Fw	Forward	CGTCGCCGTCCAGCTCGACCAGCTTCATCCTCAAACCATCTCTGA	<i>Mtmr14</i> Exon 17
Mtmr14_Rv	Reverse	CCACTGTGCTGCTGTATGC	<i>Mtmr14</i> Exon 19
Ndor1_Fw	Forward	CGTCGCCGTCCAGCTCGACCAGCCCTGGGTAGGAGATCTTT	<i>Ndor1</i> Exon 4
Ndor1_Rv	Reverse	GCTGGCTATGTTGAGCTCCT	<i>Ndor1</i> Exon 5
Trmt6_Fw	Forward	CGTCGCCGTCCAGCTCGACCAGTGAAGCCATCTACCCGTATTC	<i>Trmt6</i> Exon 5

(Continued on next page)

Continued

Primer name	Orientation	Sequence	Target
Trmt6_Rv	Reverse	CCATCATGGCACCTAGCAC	<i>Trmt6</i> Exon 6
tdTomato_Fw	Forward	ACATGGCCGTCATCAAAGA	<i>dtTomato</i>
tdTomato_Rv	Reverse	CTTGACAGCTCGTCCATGC	<i>dtTomato</i>
Acer3_Fw	Forward	CGTCGCCGTCCAGCTCGACCAGTCATGTATGGAATGTTGGTCTTT	<i>Acer3</i> Exon 7
Acer3_Rv	Reverse	TCAGTGAATCACAAAAGATGTTATC	<i>Acer3</i> Exon 9
Gpt2_Fw	Forward	CGTCGCCGTCCAGCTCGACCAGCTGAGGTAATCCGAGCCAAC	<i>Gpt2</i> Exon 3
Gpt2_Rv	Reverse	AAATACCGTCGCTAGCTCCA	<i>Gpt2</i> Exon 5
Peli1_Fw	Forward	CGTCGCCGTCCAGCTCGACCAGCCCAAACGGTGATAGAGGAA	<i>Peli1</i> Exon 3
Peli1_Rv	Reverse	CGTCTGGGCTCGAGATAAAG	<i>Peli1</i> Exon 4
Peli_In_Fw	Forward	CGTCGCCGTCCAGCTCGACCAGATTCAGCGTGTGTGTGTGT	<i>Peli1</i> Intron 3
Kcnp2_Ex5+6_Fw	Forward	CGTCGCCGTCCAGCTCGACCAGCGGAATTGTCAACGAGGAGA	<i>Kcnp2</i> Exon 4
Kcnp2_Ex5_Rv	Reverse	CCATCATGGTTGGTGTCAAA	<i>Kcnp2</i> Exon 5
Kcnp2_Ex6_Fw	Forward	GCCATCCTTGTGTGAGGTCAT	<i>Kcnp2</i> Exon 6
Tcof1_Fw	Forward	CGTCGCCGTCCAGCTCGACCAGAGCCAGGGAAGACAGAGGAC	<i>Tcof1</i> Exon 16
Tcof1_Rv	Reverse	CTGGACTCCTTCTGGGGTAG	<i>Tcof1</i> Exon 18
Dtnb_Fw	Forward	CGTCGCCGTCCAGCTCGACCAGTCTACATCTGCTGGCTCCAC	<i>Dtnb</i> Exon 16
Dtnb_Rv	Reverse	AAAGCCAATCAGGACACAGG	<i>Dtnb</i> Exon 18
Add1_Fw	Forward	CGTCGCCGTCCAGCTCGACCAGCCTCTGTTAAGAGCAGCAAGTG	<i>Add1</i> Exon 1
Add1_Rv	Reverse	TTGTGAGGGGCTGTGGTT	<i>Add1</i> Exon 3
Nova1_Fw	Forward	CGTCGCCGTCCAGCTCGACCAGACCTCAGACCACCGTTAATCC	<i>Nova1</i> Exon 3
Nova1_Rv	Reverse	CACAGTAGCACCTCCCTTCC	<i>Nova1</i> Exon 5
Fam171a_Fw	Forward	CGTCGCCGTCCAGCTCGACCAGTCACGTGGACGTACATTGCT	<i>Fam171a</i> Exon 6
Fam171a_Rv	Reverse	ATGTTGCCTGATCCCTCTTG	<i>Fam171a</i> Exon 8
Fbxw11_Fw	Forward	CGTCGCCGTCCAGCTCGACCAGCGGTGATTGAAGACAAGACC	<i>Fbxw11</i> Exon 1
Fbxw11_Rv	Reverse	ATGCTCTGCAGGCAACTCAG	<i>Fbxw11</i> Exon 3
Ppil4_Fw	Forward	CGTCGCCGTCCAGCTCGACCAGTGGTGATCAAGCAAGCTTTT	<i>Ppil4</i> Exon 4
Ppil4_Rv	Reverse	CCATGCCTTCTGTCACTTCA	<i>Ppil4</i> Exon 5
Adgrl3_Fw	Forward	CGTCGCCGTCCAGCTCGACCAGATGTGGCCACCACAGCTACT	<i>Adgrl3</i> Exon 1
Adgrl3_Rv	Reverse	CTGGCAGATAACACCGAATG	<i>Adgrl3</i> Exon 3
Chl1_F	Forward	CAGTGATCCAGCTTTAGGAGAAG	<i>Chl1</i> Exon 1
Chl1_R	Reverse	AAATACCACTCTCGTTCAACA	<i>Chl1</i> Exon 3
Snap25_F2	Forward	GAGGAAGGGATGGACCAAATC	<i>Snap25</i> Exon 2
Snap25_R2	Reverse	TTGTTACCCTGCGGATGAAG	<i>Snap25</i> Exon 6
Epha5_F_1	Forward	GCCAGGAGTCAGAACCTATATT	<i>Epha5</i> Exon 7
Epha5_R_1	Reverse	CACCTTCTAGATGGATGATGTTTG	<i>Epha5</i> Exon 9
Ncam1_F	Forward	TCTGAGTGGAACCGGAAATC	<i>Ncam1</i> Exon 12
Ncam1_R	Reverse	GTGTGTGTGTATGTGAGAGAGAG	<i>Ncam1</i> Exon 16

Differential Gene Expression, Alternative Splicing Analyses, and Motif Enrichment

Downstream sample demultiplexing and computational analysis were performed at the NYULMC Genome Technology Center. All the reads were mapped to the mouse reference genome (GRCm38.74/mm10) using the STAR aligner (v2.5.0c) (Dobin et al., 2013). Alignments were guided by a Gene Transfer File (Ensembl GTF version GRCm38.74) and the mean read insert sizes and their standard deviations were calculated using Picard tools (v.1.126) (<http://broadinstitute.github.io/picard/>). The Read Per Million (RPM) normalized BigWig files were generated using BEDTools (v2.17.0) (Quinlan and Hall, 2010) and bedGraphToBigWig tool (v4). For the Lhx6 E18.5-P22 time-course, approx. 55E6-80E6 reads were aligned per sample; for SST-Rbfox1 removal, approx. 40E6-70E6 reads were aligned per sample; for Tac1-Rbfox1 removal, approx. 50E6-60E6 reads were aligned per sample. The samples processed for downstream analysis were as follows: 15 samples for Lhx6 E18.5-P22 time-course (3 samples per condition), 10 samples for SST-Rbfox1 removal (5 samples per genotype) and 10 samples for Tac1-Rbfox1 removal (3 control samples, 7 cKO samples).

Transcripts were assembled using cufflinks (v2.0) (Trapnell et al., 2013) and their differential expression analysis was performed using Cuffdiff. We used rMATS (v3.0.9) (Shen et al., 2014) to study the event types such as skipped exons (SE), alternative 3' splice

sites (A3SS), alternative 5' splice sites (A5SS), mutually exclusive exons (MXE) and retained introns (RI). rMATS uses a counts-based model, detects alternative splicing events using both splice junction and exon body counts and ascribes an exon inclusion level value ψ for each event in each condition. It then determines the differential $|\Delta\psi|$ value across conditions (cut-offs for significance were placed at $p\text{-val} < 0.05$ and $|\Delta\psi| \geq 0.1$, unless stated otherwise). To compare the level of similarity among the samples and their replicates, we used two methods: classical multidimensional scaling or principal-component analysis and Euclidean distance-based sample clustering. The downstream statistical analyses and generating plots were performed in R environment (v3.1.1) (<https://www.r-project.org/>).

To assess the enrichment for the Rbfox1-binding motif in the predicted differentially regulated exons we utilized rMAPS (Park et al., 2016). We utilized the raw output from rMATS analysis (12 RNaseq experiments PV+ cINs and 8 RNaseq experiments SST+ cINs) with significant splicing events cut off at FDR > 50%. rMAPS performs position weight analysis to assess the enrichment of RNA binding protein binding motifs in the exonic and flanking intronic regions of upregulated or downregulated exons and plots the motif density along with a given pValue in comparison to unregulated exons.

Validation of Cell-Specific Rbfox1-Dependent Exons by RT-PCR

Total RNAs from sorted cINs were extracted as described above and at least three independent biological replicates were used in each experiment. RT-PCR validation of regulated exons was performed as described before (Han et al., 2014). After denaturation, samples were run on 10% Novex TBE-Urea Gels (ThermoFisher). Gels were directly scanned by ChemiDoc Imaging System (Bio-Rad) and quantified by ImageStudio program (Li-Cor).

Immunoprecipitation of RNA-Binding Protein-RNA Complexes (RIP)

For RNA immunoprecipitation (RIP), three P8 Dlx6a^{Cre/+}; Ai9^{fl/fl} (for RIP with total cellular extract) and three P8 Dlx6a^{+/+}; Ai9^{fl/fl} (for RIP with nuclear extract) mice were used. The cortex was rapidly dissected in ice cold RNase- and protease-free 1X PSB. For RIP with total cellular extract, freshly resected tissue was teased apart in ice-cold PBS using a Dounce homogenizer until a single-cell suspension was obtained. Cells were then collected by centrifugation at 1500 rpm for 5 min at 4°C and the supernatant was discarded. The pellet was then re-suspended in 200 μ l of complete RIP Lysis Buffer (Magna RIP, Millipore, Cat. # 17-700). For RIP with nuclear extract, freshly dissected pieces were transferred into a solution containing protease and RNase inhibitors, 1X spermine, 1X spermidine, 1X DTT, and 0.3% IGEPAL CA-630 and then homogenized using a Dounce homogenizer. The single cell suspension was then filtered through a 30 μ m strainer and an equal volume of a solution containing Optiprep and 50% iodixanol was added to the cell suspension and mixed. The mixture was then transferred to ultracentrifuge tubes, under-laid with a 29% iodixanol solution and centrifuged at 10,000 g for 30 min. Supernatant was removed and the pellet was re-suspended in complete RIP Lysis Buffer (Magna RIP, Millipore, Cat. # 17-700). Immunoprecipitation of RNA-binding Protein-RNA complexes as well as purification of the immunoprecipitated RNA was carried out following the manufacturer's instructions (Magna RIP, Millipore, Cat. # 17-700). 5 μ g of anti-Fox1 Antibody (clone 1D10, MABE985, Millipore) were used for each RIP reaction. Rbfox1 immunoprecipitation was verified by western blot. Briefly, samples were resolved by SDS-PAGE and transferred onto PVDF membranes. Membranes were blocked with 5% Blotting-Grade Blocker (Bio-Rad, #1706404) in TBST (20mM Tris-HCl pH7.5, 150mM NaCl and 0.1% Tween20) for 1 hr and probed with the following primary antibodies overnight at 4°C: mouse Anti- β -Actin–Peroxidase antibody (1:10000, A3854, Sigma) and mouse anti-Fox1 (1:1000, MABE985, Millipore). After incubation with VeriBlot for IP Detection Reagent (HRP) (1:200, ab131366, Abcam), protein levels were visualized by chemiluminescence. Blots were scanned using a ChemiDoc Imaging System (Bio-Rad). Purified RNA was retrotranscribed and processed as described above (validation of cell-specific Rbfox1-dependent exons by RT-PCR). RT-PCR was performed within the linear amplification phase of PCR (i.e., 20–25 cycles depending on the target).

GO Analysis

We performed GO analysis using the DAVID online Bioinformatics Resources 6.8 (Huang et al., 2009).

iCLIP Analysis

We analyzed the iCLIP data RNA-seq reads from Damianov et al. (2016) (Rbfox1-HMW- forebrain) available on GEO: GSM1835189. All of the reads were mapped to the mouse reference genome (GRCm38.74/mm10) as above, and duplicate reads were removed using Picard tools. Peak calling was performed using MACS (v1.4.2) (Zhang et al., 2008) and peak count tables were created using BEDTools (Quinlan and Hall, 2010). Differential binding analysis was performed using DESeq2. ChIPseeker (v1.8.0) (Yu et al., 2015) and R package were used for peak annotations and. The RPM normalized BigWig files were generated using MACS and wigToBigWig.

QUANTIFICATION AND STATISTICAL ANALYSIS

In all figures: * $p < 0.05$; ** $p < 0.01$; *** $p < 0.001$; **** $p < 0.0001$. Statistical analyses for differential gene expression and alternative splicing changes were performed using rMATS. To quantify the layer distribution and density of various populations of cortical interneuron, the proportion of interneurons of given subtypes over the total number of fate-mapped interneurons across cortical layers was calculated in at least three cryostat tissue sections from a minimum of three individual brains. Thus, percentages presented

in Figures 2 and 4 were calculated by dividing the number of markerX+/reporter+ neurons in each layer (eg, layer I, layerII/III, layerIV and layerV/VI) by the total number of reporter+ neurons. Percentages were compared with repeated t tests in *GraphPad Prism*, and means \pm (standard deviation, SD) are represented.

DATA AND SOFTWARE AVAILABILITY

The accession number for the RNA sequencing data reported in this paper is NCBI GEO: GSE119998.